PHYSICAL PROPERTIES OF EMISSION-LINE GALAXIES AT z similar to 2 FROM NEAR-INFRARED SPECTROSCOPY WITH MAGELLAN FIRE

Daniel Masters, Patrick Mccarthy, Brian Siana, Mathew Malkan, Bahram Mobasher, Hakim Atek, Alaina Henry, Crystal L. Martin, Marc Rafelski, Nimish P. Hathi, et al.

Draft version September 18, 2018
Preprint typeset using LaTeX style emulateapj v. 5/2/11

PHYSICAL PROPERTIES OF EMISSION-LINE GALAXIES AT $Z \sim 2$ FROM NEAR-INFRARED SPECTROSCOPY WITH MAGELLAN FIRE

Daniel Masters[1,2], Patrick McCarthy[2], Brian Siana[1], Mathew Malkan[3], Bahram Mobasher[1], Hakim Atek[4], Alaina Henry[5], Crystal L. Martin[6], Marc Rafelski[11], Nimish P. Hathi[8], Claudia Scarlata[7], Nathaniel R. Ross[3], Andrew J. Bunker[9], Guillermo A. Blanc[2], Alejandro G. Bedregal[10], Alberto Domínguez[1], James Colbert[11], Harry Teplitz[12], Alan Dressler[2]

Draft version September 18, 2018

ABSTRACT

We present results from near-infrared spectroscopy of 26 emission-line galaxies at $z \sim 2.2$ and $z \sim 1.5$ obtained with the Folded-port InfraRed Echellette (FIRE) spectrometer on the 6.5-meter Magellan Baade telescope. The sample was selected from the WFC3 Infrared Spectroscopic Parallels (WISP) survey, which uses the near-infrared grism of the Hubble Space Telescope Wide Field Camera 3 to detect emission-line galaxies over $0.3 \lesssim z \lesssim 2.3$. Our FIRE follow-up spectroscopy (R$\sim$5000) over 1.0–2.5 μm permits detailed measurements of physical properties of the $z \sim 2$ emission-line galaxies. Dust-corrected star formation rates for the sample range from $\sim$5–100 $M_\odot$ yr^{-1} with a mean of 29 $M_\odot$ yr^{-1}. We derive a median metallicity for the sample of 12 + log(O/H) = 8.34 or $\sim$0.45 $Z_\odot$. The estimated stellar masses range from $\sim 10^{8.5} - 10^{9.5}$ $M_\odot$, and a clear positive correlation between metallicity and stellar mass is observed. The average ionization parameter measured for the sample, $\log U \approx -2.5$, is significantly higher than what is found for most star-forming galaxies in the local universe, but similar to the values found for other star-forming galaxies at high redshift. We derive composite spectra from the FIRE sample, from which we infer typical nebular electron densities of $\sim$100-400 cm^{-3}. Based on the location of the galaxies and composite spectra on BPT diagrams, we do not find evidence for significant AGN activity in the sample. Most of the galaxies as well as the composites are offset in the BPT diagram toward higher [O III]/Hβ at a given [N II]/Hα, in agreement with other observations of $z \gtrsim 1$ star-forming galaxies, but composite spectra derived from the sample do not show an appreciable offset from the local star-forming sequence on the [O III]/Hβ versus [S II]/Hα diagram. We infer a high nitrogen-to-oxygen abundance ratio from the composite spectrum, which may contribute to the offset of the high-redshift galaxies from the local star-forming sequence in the [O III]/Hβ versus [N II]/Hα diagram. We speculate that the elevated nitrogen abundance could result from substantial numbers of Wolf-Rayet stars in starbursting galaxies at $z \sim 2$.

1. INTRODUCTION

The rest-frame optical spectra of star-forming galaxies at all redshifts exhibit emission lines from which detailed physical properties can be inferred. For galaxies at the peak of cosmic star formation at $z \sim 2$, these emission lines are shifted into the near-infrared, which, combined with the intrinsic faintness of the sources, makes them difficult to observe from the ground. For this reason, relatively few near-infrared spectra of galaxies at $z \sim 2$ that cover all of the important rest-frame optical emission lines have been published to date (e.g., Erb et al. 2006; Hainline et al. 2009; Erb et al. 2010; Rigby et al. 2011; Belli et al. 2013).

The available near-infrared spectra of star-forming galaxies at $z \sim 2$ have revealed differences in comparison with counterparts in the local universe (Liu et al. 2008; Newman et al. 2013). For example, star-forming galaxies at $z \sim 2$ tend to have higher [O III]/Hβ ratios at a given [N II]/Hα ratio than local star-forming galaxies. This observation has been attributed to more extreme interstellar medium (ISM) conditions, on average, in galaxies at high redshift, possibly as a result of higher nebular electron densities, harder ionizing radiation fields, different gas volume filling factors, or some combination of these (Shapley et al. 2005; Brinchmann et al. 2008b; Shirazi et al. 2013; Kewley et al. 2013a,b). The clumpy morphology and relatively high velocity dispersions observed in many of these sources (Pettini et al. 2001; Förster Schreiber et al. 2006; Genzel et al. 2008; Law et al. 2009) may support the conjecture that star-formation in the early universe generally occurs in denser and higher pressure environments than those found in local star-forming galaxies. Significant contribution of active galactic nuclei (AGN) to emission line fluxes for

[1] Department of Physics and Astronomy, University of California, Riverside, CA 92521
[2] Carnegie Observatories, Pasadena, CA 91101
[3] Department of Physics and Astronomy, UCLA, Los Angeles, 90095
[4] Laboratoire d'Astrophysique Ecole Polytechnique Fédérale, Sauverny, Switzerland
[5] Astrophysics Science Division, Goddard Space Flight Center, Greenbelt, MD 20771
[6] Department of Physics, Universitey of California, Santa Barbara, CA 93106
[7] Department of Physics and Astronomy, University of Minnesota
[8] Aix Marseille Université, CNRS, LAM (Laboratoire d'Astrophysique de Marseille) UMR 7326, 13388, Marseille, France
[9] Department of Physics, University of Oxford, UK
[10] Department of Physics and Astronomy, Tufts University, Medford, MA 02155
[11] Spitzer Science Center, California Institute of Technology, Pasadena, CA 91125, USA
[12] Infrared Processing and Analysis Center, Caltech, Pasadena, CA 91125

$z \sim 2$ galaxies has also been suggested as a source of the elevated line ratios (Trump et al. 2011, 2013).

The slitless grism spectroscopy provided by the Wide Field Camera 3 (WFC3) on the Hubble Space Telescope (HST) has enabled the discovery of large numbers of star-forming galaxies near the peak of cosmic star formation (Atek et al. 2010, 2011; Straughn et al. 2011; van der Wel et al. 2011; Trump et al. 2011; Brammer et al. 2012). Grism surveys such as the WFC3 Infrared Spectroscopic Parallels (WISP) survey (Atek et al. 2010) are well-suited to finding low-mass star-forming galaxies at intermediate redshifts through their optical emission lines. While WFC3 grism spectroscopy detects large numbers of emission-line galaxies, it is not ideal for extracting the physical information encoded in their optical spectra. The spectral resolution ($R \sim 130$ in G141 and $R \sim 210$ in G102) is insufficient to resolve Hα from [N II]λ6548, 6583, or detect line broadening due to AGN activity. Moreover, despite the broad wavelength coverage ($\sim$0.8–1.7 μm) of the grism, Hα is not detected for galaxies at $z \gtrsim 1.6$ and important metallicity diagnostics such as $R_{23} \equiv ([\text{O III}]\lambda 4959, 5007 + [\text{O II}]\lambda 3727)/\text{H}\beta$ are often inaccessible. For these reasons, ground-based spectroscopy with the new generation of near-infrared spectrometers is required to constrain the physical properties of these galaxies.

Here we present rest-frame optical spectroscopy of 26 emission-line galaxies from WISP obtained with the Folded-port Infrared Echellette (FIRE, Simcoe et al. 2008, 2010) on the Magellan Baade 6.5 meter telescope. The sample consists of 13 sources at $z \sim 2.2$ and 13 at $z \sim 1.5$. Galaxies in the sample were selected from the WISP survey based on the detection of strong [O III]λ5007 emission (at $z \sim 2.2$) or Hα (at $z \sim 1.5$) in the G141 grism data. Follow-up near-IR spectroscopy with FIRE enables us to: (1) detect Hα for sources at $z > 1.6$ and split Hα and [N II] in order to determine star formation rates (SFRs), (2) get accurate dust reddening estimates using the Balmer decrement, (3) infer metallicities and ionization parameters from strong lines, (4) measure diagnostic line ratios to test for nuclear activity, and (5) resolve emission line velocity dispersions. We also construct composite spectra from our sample, which allow us to investigate the statistical properties of strongly star-forming galaxies at $z \sim 2.2$ and $z \sim 1.5$ in greater detail.

This paper is structured as follows. In §2 we provide an overview of the WISP survey and the emission-line galaxies selected for follow-up spectroscopy. In §3 we discuss the Magellan FIRE spectroscopy and data reduction. In §4 we present the physical properties measured from the FIRE spectra, including dust obscuration, metallicity, ionization parameter, star formation rate and kinematics. In §5 we discuss the composite spectrum derived from the sample. In §6 we analyze the results, exploring the implications of our findings for the nature of starbursting galaxies at $z \sim 2$. In §7 we conclude with a discussion. We adopt a cosmology with $\Omega_M = 0.3$, $\Omega_\Lambda = 0.7$ and $H_0 = 70$ km s^{-1} Mpc^{-1}.

2. WFC3 DATA & SAMPLE SELECTION

2.1. *WISP Survey*

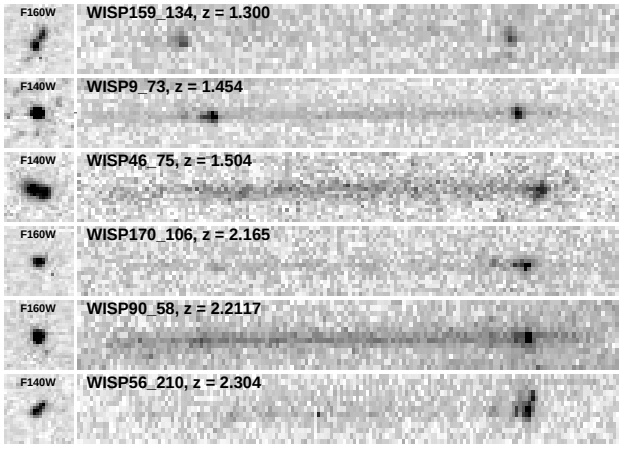

FIG. 1.— Examples of the WISP sources selected for follow-up Magellan FIRE spectroscopy. The direct WFC3 H-band images on the left are 3″ on a side. Prominent rest-frame optical emission lines are visible in the G141 grism exposures, which span 1.1-1.7 μm.

The WISP team (PI Malkan, Atek et al. 2010) is obtaining slitless, near-infrared grism spectroscopy over 0.8–1.7 μm using the two infrared grisms installed on the IR channel of Wide Field Camera 3 (WFC3; Kimble et al. 2008), with more than 800 arcmin^2 of sky covered at present. WFC3 grism observations are highly sensitive to emission-line galaxies over $0.3 \lesssim z \lesssim 2.3$, without suffering from the observational biases affecting ground-based surveys at these redshifts.

WISP is a "pure parallel" program, which means that the WFC3 pointings are determined by primary observing programs using other HST instruments. The WFC3 observations are taken in a parallel field determined by the offset of the instruments on the focal plane and the roll angle of the telescope. WISP consists of two types of observations: a deep survey for parallel targets with more than four orbits of visibility, covering a relatively small number of fields, and a shallower survey for parallel targets with one to three orbits of visibility, covering a much larger number of fields. Parallel observing targets are selected at galactic latitudes $|b| > 20°$ with a preference for longer visibility times. Typical integration times for a 4–5 orbit target are $\sim$5000 seconds in G102 and $\sim$2000 seconds in G141. Longer parallel opportunities are also imaged in F110W and UVIS (the F475X and/or F600LP filters). The shallower WISP fields are restricted to the G141 grism and H-band imaging, with a typical G141 integration time for a 2-orbit target of $\sim$4000 sec. Because the 2–3 orbit pointings typically achieve deeper G141 integrations and cover a larger area than the deep survey, a substantial fraction of the emission-line galaxies studied here were selected in these fields.

2.2. *Source Selection*

We select galaxies in WISP fields at $z \sim 2.2$ and $z \sim 1.5$ with clearly detected emission lines. These redshifts were chosen because Hα and other important rest-frame optical emission lines are redshifted into relatively clear atmospheric windows for ground-based near-IR spectroscopy. To find the candidates, the WFC3 2D G141 grism frames were examined carefully to iden-

TABLE 1
Overview of the emission-line galaxies from the WISP survey selected for follow-up near-IR spectroscopy with FIRE.

Object ID	R.A. (J2000)	Decl. (J2000)	z	EW([O III])[a] (Rest Å)	EW(Hα)[b] (Rest Å)	F110W (AB mag)	F140W (AB mag)	F160W (AB mag)
WISP159_134	20:56:30.91	–04:47:56.3	1.300	···	314 (36)	···	···	22.82 (0.03)
WISP134_171	18:42:33.21	–68:58:37.4	1.354	124 (6)	266 (11)	···	···	22.55 (0.02)
WISP50_65	22:22:15.86	+09:36:47.1	1.437	···	202 (15)	···	22.35 (22.06)	···
WISP173_205	01:55:23.64	–09:03:10.2	1.444	982 (146)	603 (42)	···	···	23.71 (0.03)
WISP9_73	12:29:43.35	+07:48:35.9	1.454	233 (9)	221 (12)	22.80 (0.02)	22.79 (0.02)	···
WISP43_75	21:04:06.18	–07:22:28.6	1.482	···	137 (14)	22.62 (0.16)	22.37 (0.02)	···
WISP25_53	10:08:44.82	+07:10:20.4	1.486	···	130 (7)	···	22.20 (0.01)	···
WISP46_75	22:37:56.48	–18:42:46.1	1.504	···	245 (28)	···	22.77 (0.20)	···
WISP126_90	13:41:49.16	+05:03:06.2	1.536	···	···	···	···	22.26 (0.02)
WISP22_111	08:52:46.09	+03:09:19.4	1.541	87 (15)	···	···	22.60 (0.03)	···
WISP22_216	08:52:46.29	+03:08:45.9	1.543	99 (8)	···	···	23.93 (0.06)	···
WISP64_2056	14:37:30.20	–01:50:51.4	1.610	···	···	27.45 (0.20)	···	25.12 (0.20)
WISP81_83	01:10:06.69	–02:23:06.5	1.677	122 (11)	···	23.11 (0.20)	···	23.30 (0.06)
WISP138_173	15:45:31.03	+09:33:30.0	2.158	286 (22)	···	···	···	23.48 (0.05)
WISP170_106	00:12:28.18	–10:28:33.6	2.165	154 (7)	···	···	···	23.31 (0.03)
WISP64_210	14:37:28.34	–01:49:54.4	2.177	143 (14)	···	24.55 (0.05)	···	23.66 (0.06)
WISP204_133	11:19:46.37	+04:10:30.8	2.191	226 (44)	···	···	23.93 (0.05)	···
WISP27_95	11:33:08.67	+03:28:27.0	2.192	150 (14)	···	23.66 (0.25)	23.03 (0.05)	···
WISP147_72	23:58:22.06	–10:14:48.7	2.196	131 (16)	···	22.99 (0.01)	···	22.03 (0.02)
WISP90_58	01:00:56.20	+02:25:54.0	2.212	71 (4)	···	···	···	22.53 (0.02)
WISP70_253	04:02:02.50	–05:37:19.5	2.215	257 (23)	···	···	24.67 (0.48)	···
WISP175_124	03:42:19.72	–20:33:17.1	2.216	271 (18)	···	···	23.74 (0.05)	···
WISP96_158	02:09:26.37	–04:43:29.0	2.234	238 (10)	···	24.08 (0.31)	···	23.61 (0.04)
WISP138_160	15:45:36.29	+09:34:26.7	2.264	116 (4)	···	···	···	23.30 (0.03)
WISP56_210	16:16:50.44	+06:36:38.0	2.304	372 (13)	···	···	23.84 (0.03)	···
WISP206_261	10:34:17.56	–28:30:49.8	2.315	210 (28)	···	···	24.26 (0.08)	···

[a] Rest-frame equivalent widths derived from the WFC3 G141 grism data.
[b] 1σ errors shown in parentheses here and throughout the paper.

tify sources with the prominent [O III]λ4959, 5007 emission line complex and/or Hα for sources at $z \sim 1.5$. Line fluxes were measured to ensure that FIRE spectroscopic follow-up would be feasible; all sources were required to have [O III]λ5007 or Hα fluxes greater than 5×10^{-17} erg cm^{-2} s^{-1}. The WFC3 data for the emission-line galaxy sample are summarized in Table 1, and examples of the WFC3 H-band direct imaging and G141 2D spectra are shown in Figure 1.

The grism selection used here is particularly sensitive to star-forming galaxies with high equivalent width (EW) emission lines, which tends to favor lower mass, younger systems, with high specific star formation rates (sSFRs). The relation of our emission-line galaxy selection to galaxies selected using photometric techniques at similar redshifts, for example the "BX/BM" (Steidel et al. 2004), "BzK" (Daddi et al. 2004) and UV-dropout (Hathi et al. 2010) samples, is uncertain. It has been shown previously that the different color cut prescriptions non-uniformly sample the true population of galaxies (Reddy et al. 2005; Quadri et al. 2007; Grazian et al. 2007; Ly et al. 2011), although there is large overlap between the galaxies selected with each method. The overlap of our sample with the UV color-selected galaxies at similar redshift is likely high, although the grism-selected emission-line sample can probe lower mass galaxies due to its relative insensitivity to the galaxy continuum.

3. MAGELLAN FIRE NEAR-IR SPECTROSCOPY

3.1. *Observations & Data Reduction*

Observations with Magellan FIRE were conducted over six observing runs from April 2011 to March 2013. FIRE was used in high-resolution echelle mode to give near-infrared spectra spanning $\sim$1.0 – 2.5 μm. The success rate was nearly 100% for the candidates, with the only non-detections occurring in poor observing conditions. Observations were conducted as follows. The J-band acquisition camera was used to locate a nearby star from which a blind offset was applied to position the science target in the slit. The slits used were either 0.6″, 0.75″ or 1.0″ in width, depending on the seeing, and were oriented at the parallactic angle in most cases to minimize differential atmospheric refraction. Exposure times of 900 seconds were used for sequences of ABBA dither sequences with total integrations ranging from 1 to 3.5 hours. Readouts were performed with the Sample Up The Ramp (SUTR) mode in order to minimize overheads. For each science target, at least one A0V star was observed at similar airmass for telluric correction.

Data were reduced using the publicly available pipeline[†] developed by the instrument team. A brief summary of the reduction process follows. First, the edges of the 2D echelle orders were traced and the flat field was derived using a combination of internal quartz lamp exposures and sky flat exposures. ThAr arc lamp exposures were used to derive the wavelength solution, which was then refined using the OH sky lines from the science frames. Sky subtraction was performed using the method described in Kelson (2003). In most cases optimal extraction was used to derive the 1D spectrum from the 2D frames, after fitting a spatial profile to a prominent emission line in a 2D frame. The 1D spectra were flux calibrated using observations of an A0V telluric standard star, and then combined to obtain the final, flux calibrated 1D spectrum. Examples of reduced FIRE 1D

[†] http://web.mit.edu/~rsimcoe/www/FIRE/ob_data.htm

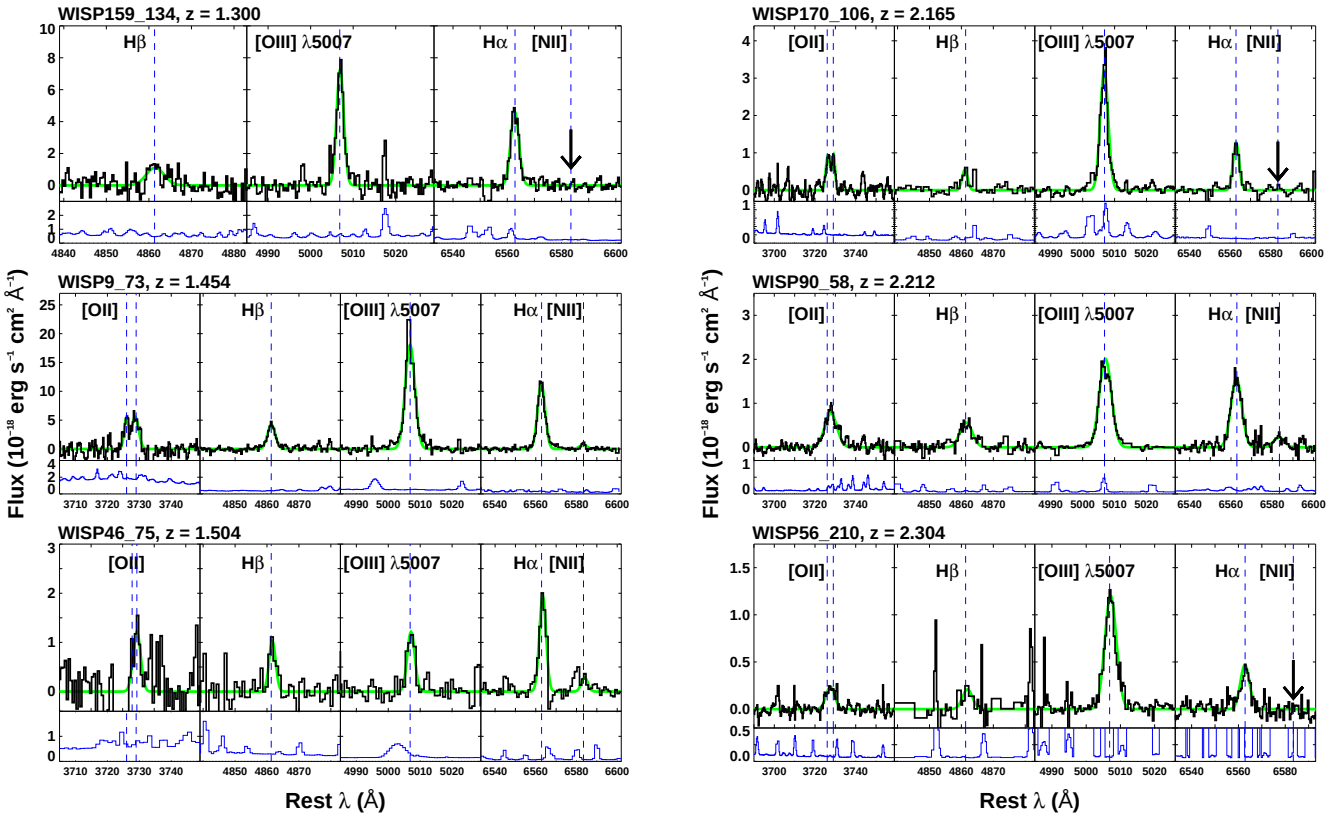

FIG. 2.— Example 1D spectra from Magellan FIRE, for the same sources as in Figure 1. On the left are spectra from the $z \sim 1.5$ sample and on the right are spectra from the $z \sim 2.2$ sample. Fits are overlaid in green and the emission lines are labeled. Downward arrows indicate non-detections. The lower panels show the error spectra. The appendix contains WFC3 and FIRE data for all objects in the sample.

spectra are shown in Figure 2, and the entire sample is shown in the Appendix.

3.1.1. *Absolute flux calibration*

The emission line fluxes measured from the FIRE 1D spectra frequently were lower by a factor of 2-4 compared to the same lines measured from the G141 grism spectra. When multiple lines were measured with both instruments, for example [O III]λ5007 and Hα for galaxies at $z \sim 1.5$, the ratio of the FIRE and WFC3 line fluxes was found to be consistent for the two lines to within 20%, indicating that the relative calibration of FIRE is reliable. The exact reason for the absolute offset is unclear, but is probably a combination of slit losses in FIRE and difficulty in deriving the absolute correction for sources with essentially no detected continuum.

For the majority of the analysis presented here we do not require absolute line flux values, but to infer SFRs for the sample we do need to know the absolute flux of Hα. We use the WFC3 measurements to derive the absolute Hα flux. For galaxies at $z \sim 1.5$ we take the WFC3-measured F(Hα) as the reference value, after correcting for blended F([N II]) as measured from the FIRE spectrum. For galaxies at $z \sim 2.2$, Hα was not measured with WFC3, so we scale the measured FIRE F(Hα) by the ratio of the WFC3-measured F([O III]) to the FIRE-measured F([O III]), which is justified given the consistent relative calibrations of the two instruments.

3.2. *Line Measurement*

We fit the emission lines with Gaussian profiles using the IDL MPFIT routines (Markwardt 2009). Errors in the derived line fluxes and velocity dispersions were determined using Monte Carlo simulations in which the lines were fit repeatedly after applying gaussian noise consistent with the error spectrum. The [N II]λ6583 flux was fit simultaneously with Hα while fixing the width and separation of the two lines. For non-detected [N II]λ6583, the 95% confidence upper limit on the flux was determined with a Monte Carlo simulation in which noise was added to the spectrum and the [N II] flux was fit repeatedly as described. The resulting distribution of [N II] fluxes determined the 2σ upper limit. This limit was verified by adding in and attempting to recover known fluxes in empty regions of the spectrum near [N II]λ6583.

The instrumental resolution of FIRE was determined by measuring the FWHM values of multiple ThAr lines. This was done for slit widths of 0.6″, 0.75″, and 1.0″, giving FWHM resolutions of 59, 65.5, and 72 km s^{-1}, respectively. These values would be appropriate for galaxies that fill the slit uniformly; in reality the resolution may be lower depending on the light profile of the target. Galaxy line widths are considered to be resolved when the measured FWHM of the line was at least twice the instrumental resolution. We find that all of the emission lines are resolved. Measured line fluxes are presented in Table 2 and the velocity dispersions for [O III]λ5007 and Hα are presented in Table 5.

4. PHYSICAL PROPERTIES OF THE SAMPLE

4.1. *Dust Extinction*

Dust preferentially attenuates shorter-wavelength light and must be taken into account when deriving physical properties from emission lines. We use the ratio Hα/Hβ (the Balmer decrement) to estimate the nebular dust extinction of galaxies in the sample. The Balmer decrement is relatively insensitive to temperature and should equal 2.86 in the absence of dust, given reasonable assumptions for the physical conditions of the H II regions producing the line emission (Osterbrock & Ferland 2006).

In computing the nebular extinction from the Balmer decrement we follow the method outlined in Momcheva et al. (2013) and Domínguez et al. (2013), which uses the extinction curve of Calzetti et al. (2000) to convert the observed Balmer decrement into $E(B-V)$ and total extinction values. The Balmer decrements we measure for the sample and the derived $E(B-V)$ and $A_{H\alpha}$ values are given in Table 3. The nebular extinctions for the sample are generally low, ranging from no evidence for extinction up to $A_{H\alpha} = 2.53$ mags, with an average extinction of $A_{H\alpha} = 0.7$ mags. In this analysis we do not correct for the possible effect of stellar absorption lines on the measured line fluxes due to the lack of reliable continuum measurements for most objects. This may affect the measured Balmer decrements and lead to slightly overestimated dust extinctions, but the effect will be small for high-EW galaxies. For example, the typical equivalent width of the stellar absorption in Hβ is 3-4 Å (see, e.g., Domínguez et al. 2013), whereas the equivalent widths of the Hβ lines in this sample are likely to be $\gtrsim$ 30 Å judging from the measured EW([O III]) values and [O III]/Hβ ratios. We conclude that the effect will not have a substantial impact on the results.

On the left panel of Figure 3 we show the Balmer decrement as a function of the observed Hα luminosity (which was scaled to account for the uncertain absolute FIRE calibration, as described in §3.1.1). There is no obvious trend between the Balmer decrement and the observed $L_{H\alpha}$, which is unsurprising given the relatively narrow range of observed Hα luminosities in our sample. Nevertheless, the Balmer decrements we find for $\log_{10}(L_{H\alpha}) \sim 42 - 42.5$ erg s^{-1} are in good agreement with those found by Domínguez et al. (2013) using stacked WFC3 spectra from WISP.

On the right panel of Figure 3 we show the inferred $E(B-V)$ values plotted against the extinction-corrected Hα luminosities. There is circularity in this plot, in that the reddening on the y-axis was used to estimate the correction for the Hα luminosity on the x-axis. If taken at face value, a clear trend is evident, with the galaxies that are more luminous in Hα having more dust extinction. This result is consistent with the trend seen at both low and high redshift that more luminous galaxies tend to have more dust obscuration (Domínguez et al. 2013), as well as with previous studies (e.g., Ly et al. 2011) that have found that the star formation rate density at $z \sim 2$ is dominated by a less numerous population of highly dust-extinguished galaxies. A word of caution is in order, however, as this might be a selection effect due to the grism selection missing obscured sources with lower intrinsic Hα luminosities.

4.2. *Metallicity*

A number of different metallicity calibrations based on emission line strengths have been proposed in the literature (see Kewley & Ellison 2008 for an overview). One of the most commonly used indicators, R_{23}, is based on the ratio ([O III]λ4959,5007+[O II]λ3727)/Hβ (Pagel et al. 1979; McGaugh 1991; Kewley & Dopita 2002; Kobulnicky & Kewley 2004). A well-known difficulty with R_{23} is that it is double-valued with 12+log(O/H), making it necessary to determine which "branch" of the R_{23} curve a galaxy is on (Dopita et al. 2013 and references therein). The R_{23} calibration also has a strong dependence on ionization parameter, although this quantity can be measured from the ratio [O III]/[O II] when R23 is observed. Another well-known metallicity indicator is $N2 \equiv \log([\text{N II}]\lambda6583/\text{H}\alpha)$ (Pettini & Pagel 2004). This estimator has the advantage of increasing monotonically with metallicity below $12 + \log(\text{O/H}) \sim 9.2$, but is also sensitive to ionization parameter (Kewley & Dopita 2002).

We find unusually large R_{23} values compared with local samples for about half of the sources for which we were able to measure R_{23}. We illustrate this in Figure 4, in which the dust-corrected R_{23} values from the FIRE sample are plotted against the ratio log([N II]/Hα). This plot is similar to the BPT diagram, but in this case both axes are commonly-used metallicity indicators. Noteworthy is the offset of many of the FIRE-observed points to higher R_{23} values at a given [N II]/Hα ratio compared with the Sloan Digital Sky Survey (SDSS; Abazajian et al. 2009) data points shown for comparision. Calibrations in the literature generally do not account for such high values. We are relatively confident that the majority of the high R_{23} values are not due to AGN activity, a point that is discussed further in §6.1.

We used the code Inferring Metallicities (Z) and Ionization parameters (IZI, Blanc et al. in prep) to further analyze the sample. This software uses Bayesian inference to compute the joint and marginalized posterior probability distribution functions (PDF) for the metallicity and ionization parameter by comparing the dust-corrected line fluxes to the predictions of a photoionization model grid. We used the grids of Levesque et al. (2010), which have been recently extended to higher ionization parameter values by Richardson et al. (2013). Again, we find that the model grids are often unable to reproduce the observed lines for those sources with high [O III]/Hα and [O III]/Hβ line ratios.

To estimate metallicities, we use the $N2$ calibration of Pettini & Pagel (2004). We then use these estimates to determine which branch of the R_{23} curve to adopt when computing the R_{23} metallicity, with the lower branch being used for $N2$ metallicities less than 8.4. The metallicity estimates from R_{23} and $N2$ are given in Table 4. In cases for which R_{23} was higher than normal, we approximate the R_{23} metallicity as $12 + \log(\text{O/H}) \sim 8.4$, the value at the nominal turnover of the R_{23} curve.

We find a median ratio [N II]/Hα of ∼10%, in close agreement with the value of ∼12% derived from the overall composite spectrum presented in §5. The $N2$ metallicities of the sample range from <13% solar to roughly solar, with a median of 0.45 $Z_\odot$ ($Z_\odot$=8.69 in units of 12+log(O/H), Asplund et al. 2009). The R_{23}

TABLE 2
Line fluxes derived from the FIRE near-IR spectroscopy.

Object ID	F([O II]λ3727)[a]	F(Hβ)	F([O III]λ5007)	F(Hα)	F([N II]λ6583)
WISP159_134	···	13.5 (3.4)	35.6 (1.3)	40.3 (2.3)	<1.3
WISP134_171	···	···	106 (3.6)	68.3 (1.5)	7.4 (1.1)
WISP50_65	11.7 (2.1)	2.8 (1.1)	10.7 (1.1)	19.3 (0.5)	6.6 (0.3)
WISP173_205	8.9 (2.2)	7.5 (0.4)	47.0 (0.7)	22.3 (0.4)	···
WISP9_73	59.4 (7.5)	31.6 (1.3)	168 (3.0)	128 (1.0)	8.2 (0.8)
WISP43_75	···	88.8 (4.8)	···	296 (37)	76.8 (20)
WISP25_53	65.9 (3.0)	31.0 (0.9)	78.9 (0.8)	86.9 (0.9)	15.8 (0.9)
WISP46_75	18.5 (3.7)	6.6 (1.1)	9.0 (0.5)	20.1 (0.7)	3.0 (0.3)
WISP126_90	···	3.8 (0.7)	···	21.9 (0.4)	8.7 (1.1)
WISP22_111	···	7.5 (1.4)	26.8 (3.3)	21.0 (0.5)	5.3 (1.0)
WISP22_216	···	11.7 (0.7)	53.6 (1.5)	32.7 (1.6)	< 0.5
WISP64_2056	14.3 (8.0)	···	30.6 (0.4)	16.9 (0.4)	< 0.6
WISP81_83	···	···	220 (4.1)	136 (1.6)	···
WISP138_173	9.2 (0.5)	2.7 (0.3)	14.5 (0.6)	16.0 (1.3)	<1.0
WISP170_106	13.2 (1.6)	3.7 (0.4)	32.0 (1.4)	15.0 (0.5)	< 1.3
WISP64_210	29.9 (1.9)	20.1 (1.4)	136 (2.3)	84.5 (3.5)	15.1 (3.7)
WISP204_133	4.3 (0.8)	2.6 (0.3)	5.7 (0.7)	3.9 (0.4)	< 0.9
WISP27_95	50.0 (1.4)	18.6 (0.7)	91.0 (0.7)	77.5 (1.2)	9.6 (1.2)
WISP147_72	14.4 (7.8)	···	86.5 (0.5)	20.2 (0.7)	1.3 (0.6)
WISP90_58	18.7 (0.8)	8.7 (0.3)	30.7 (0.5)	33.0 (0.8)	4.7 (0.4)
WISP70_253	4.1 (0.6)	7.3 (0.3)	30.1 (0.2)	14.0 (0.6)	< 0.6
WISP175_124	13.1 (0.7)	···	38.1 (0.3)	25.4 (0.9)	2.5 (0.4)
WISP96_158	19.7 (2.5)	9.0 (1.6)	94.4 (2.3)	44.9 (1.8)	< 2.9
WISP138_160	···	49.8 (5.7)	256 (1.6)	170 (1.5)	14.6 (1.2)
WISP56_210	4.2 (0.3)	2.7 (0.4)	16.9 (0.7)	7.5 (1.2)	···
WISP206_261	6.9 (1.5)	7.4 (0.5)	49.1 (0.4)	30.3 (0.9)	< 1.1

[a] All fluxes are in units of 10^{-18} erg cm^{-2} s^{-1}. Fluxes presented here have not been scaled to match WFC3 fluxes, as described in §3.1.1

metallicities are similar, with a median metallicity of 0.50 Z$_\odot$. As pointed out by Dopita et al. (2013), R_{23}-based metallicities should be treated with caution, particularly as the ratio is only weakly sensitive to abundance for $8.3 \lesssim 12 + \log(\mathrm{O/H}) \lesssim 9.0$. Therefore, we use the $N2$ metallicities in the analysis that follows, although these can also be problematic.

Both Villar et al. (2008) and Cowie et al. (2011) have shown a strong relationship between the [N II]/Hα ratio and EW(Hα) for star-forming galaxies at lower redshifts. For most of our sample we are unable to determine EW(Hα), but the [N II]/Hα ratios we find are consistent with EW(Hα) values of ∼100–300 as determined by those authors. Based on the few sources for which we do have EW(Hα), this is very reasonable. In Figure 5 we plot the [N II]/Hα ratio against EW([O III]λ5007) as a proxy for EW(Hα). A negative correlation of EW([O III]) and log([N II]/Hα) is evident. Assuming EW([O III]) is a rough tracer of age, as is the case for EW(Hα), the increasing [N II]/Hα ratio with decreasing EW([O III]) may reflect a smooth metal buildup with age.

4.2.1. *Mass-metallicity relation*

The relationship between the gas-phase metallicity and the stellar mass of galaxies has been explored extensively in the literature because it directly constrains models of the interplay between star formation, pristine gas inflows, chemical enrichment of the ISM, and feedback in the form of supernova-driven galactic-scale winds (e.g., Lequeux et al. 1979; Skillman 1989; Zaritsky et al. 1994; Tremonti et al. 2004; Erb et al. 2006; Henry et al. 2013). It is now well-established that a strong positive correlation exists between metallicity and stellar mass in both the local (Tremonti et al. 2004) and high redshift (Erb et al. 2006) universe. This relationship probably reflects the higher gas fractions found in lower mass systems and/or the relative inability of low-mass galaxies to retain metals accelerated by supernova-driven winds. The mass-metallicity relation at $z \sim 2$ was recently explored at lower masses than previously possible using stacked data from the WISP survey (Henry et al. 2013). We explore this regime further using our FIRE data.

On the left panel of Figure 5 we show the $N2$ metallicities plotted against the rest-frame V band absolute magnitudes derived from WFC3 H band photometry (either the F140W or F160W filter), corrected for emission line contamination. There is a clear positive correlation between metallicity and luminosity. On the right panel of Figure 5 we show the $N2$-based metallicity estimates against rough stellar mass estimates from the WFC3 photometry. The masses were estimated by using a M/L ratio in V band from the Bruzual & Charlot 2003 (BC03) models assuming constant star-formation and an age of 100 Myr. The age was chosen to roughly match the values of EW(Hα) for the sample (the relation between age and EW(Hα) is well-known; see, e.g., Shim et al. 2011).

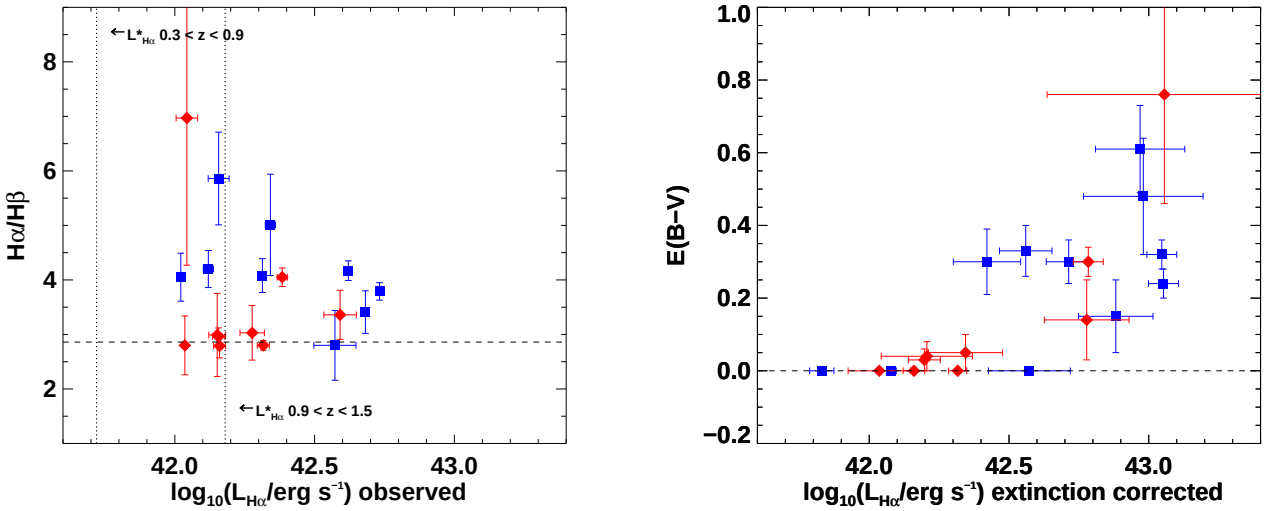

FIG. 3.— *Left:* Balmer decrement as a function of the observed Hα luminosity. The blue squares are from the $z \sim 2.2$ sample and the red diamonds are from the $z \sim 1.5$ sample. There is no trend evident here, but the values measured are consistent with the results from Domínguez et al. (2013) for this somewhat narrow range of observed $L_{\rm H\alpha}$. We indicate with dotted lines the values of $L^*_{\rm H\alpha}$ for two lower redshift intervals recently determined by Colbert et al. (2013). *Right:* The $E(B-V)$ values inferred from the Balmer decrements plotted against the extinction-corrected Hα luminosity. Here we see a clear trend, with more luminous Hα emitters having higher dust extinction. It should be noted that this plot is somewhat circular, in that the $E(B-V)$ is used to obtain the extinction corrected $L_{\rm H\alpha}$ values.

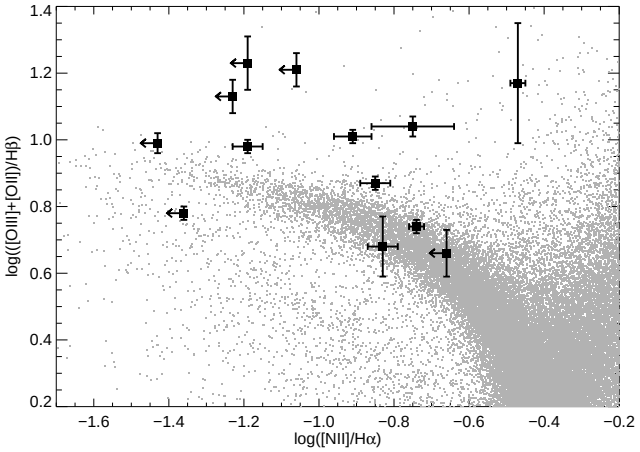

FIG. 4.— $R23$ plotted against $N2$. Both of these quantities are metallicity indicators, and in the FIRE data a hint of a turnover in R23 at low metallicities (low $N2$ values) is apparent in the two leftmost FIRE points. 60,000 data points from SDSS galaxies are shown for comparison; no turnover in R23 is apparent in this data, but this is because of the combination of the rarity of lower branch galaxies in the local universe and the lack of sensitivity of SDSS to such low-mass sources. Close to half of the galaxies in our sample show higher R_{23} values than found in local star-forming galaxies.

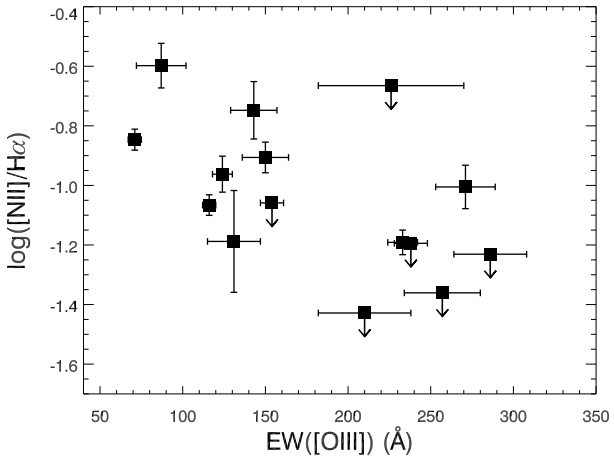

FIG. 5.— The ratio [N II]/Hα vs. EW([O III]). A fairly tight negative correlation between [N II]/Hα and EW(Hα) was shown by Cowie et al. 2011 (Figure 9f). A similar trend is apparent here, with EW([O III]) as a proxy for EW(Hα).

The large error bars primarily reflect the uncertainty in the M/L ratio, which depends on the uncertainty in the age estimates. This was in turn estimated from the likely spread in EW(Hα) values for the sample, as only a handful are directly measured from the WFC3 grism data.

The strong mass-metallicity relation we find is in relatively good agreement with the recent determination by Henry et al. (2013) using stacked WISP data at similar redshift, although that result shows a somewhat higher normalization. We also compare to the determination of the mass-metallicity relation at $z \sim 2$ from Erb et al. (2006) and find that our points show a similar trend but tend to be offset upwards from this relation. This offset may be due to a combination of the somewhat lower average redshift of points in our sample and/or a nitrogen enhancement in the emission-line sample, discussed further in §6.3. Such an enhancement, if real, could bias our $N2$ metallicity estimates toward higher values.

4.3. *Ionization Parameter*

The ionization parameter q, defined as the ratio of the flux of ionizing photons through a unit area to the local number density of hydrogen nuclei, is frequently used to characterize the radiation field in H II regions. The effective ionization parameter is defined in terms of the Strömgrem radius R_S:

$$q = \frac{Q_{H^0}}{4\pi R_S^2 n} \quad (1)$$

TABLE 3
Balmer decrements, extinctions, and SFRs for the sample.

Object ID	Hα/Hβ	*E(B-V)* (mag)	$A_{H\alpha}$ (mag)	$F(H\alpha)$ scaled[a]	$F(H\alpha)$ ext. corrected[b]	SFR (uncorr.) $M_\odot$ yr^{-1}	SFR (corr.) $M_\odot$ yr^{-1}
WISP159_134	2.99 (0.76)	$0.04^{+0.20}_{-0.04}$	0.13	14.2 (0.95)	$16.1^{+13.6}_{-2.1}$	6.6 (0.5)	$7.5^{+6.3}_{-1.0}$
WISP134_171	···	···	···	22.6 (0.78)	···	11.6 (0.4)	···
WISP50_65	6.97 (2.70)	$0.76^{+0.33}_{-0.30}$	2.53	10.0 (0.9)	103^{+180}_{-62}	6.0 (0.5)	62^{+108}_{-37}
WISP173_205	2.96 (0.16)	$0.03^{+0.05}_{-0.03}$	0.10	11.2 (0.6)	$12.3^{+2.1}_{-1.2}$	6.8 (0.4)	$7.4^{+1.3}_{-0.7}$
WISP9_73	4.05 (0.17)	$0.30^{+0.04}_{-0.04}$	1.00	18.7 (0.8)	$46.9^{+6.2}_{-5.4}$	11.5 (0.5)	$29^{+3.7}_{-3.3}$
WISP43_75	3.36 (0.45)	$0.14^{+0.11}_{-0.11}$	0.47	29.6 (3.7)	$45.5^{+18.6}_{-13.6}$	19.1 (2.4)	$29^{+12}_{-8.8}$
WISP25_53	2.80 (0.09)	$0.00^{+0.03}_{-0.00}$	0.0	15.0 (0.7)	$15.0^{+1.6}_{-0.7}$	9.8 (0.5)	$9.8^{+1.0}_{-0.5}$
WISP46_75	3.03 (0.50)	$0.05^{+0.14}_{-0.05}$	0.17	13.6 (1.3)	$15.9^{+8.6}_{-2.6}$	9.1 (0.9)	$10.6^{+5.8}_{-1.8}$
WISP126_90	5.81 (1.01)	$0.61^{+0.15}_{-0.15}$	2.03	···	···	···	···
WISP22_111	2.80 (0.54)	$0.00^{+0.16}_{-0.00}$	0.0	7.58 (0.16)	$7.6^{+4.8}_{-0.2}$	5.4 (0.1)	$5.4^{+3.4}_{-0.1}$
WISP22_216	2.79 (0.22)	$0.00^{+0.04}_{-0.00}$	0.0	9.58 (0.46)	$9.6^{+1.3}_{-0.5}$	6.8 (0.4)	$6.8^{+0.9}_{-0.4}$
WISP64_2056	···	···	···	7.68 (0.17)	···	6.1 (0.1)	···
WISP81_83	···	···	···	1.14 (0.01)	···	1.0 (0.01)	···
WISP138_173	5.86 (0.85)	$0.61^{+0.12}_{-0.12}$	2.03	9.43 (0.78)	$61.2^{+27.3}_{-18.8}$	15.3 (1.2)	99^{+44}_{-30}
WISP170_106	4.05 (0.44)	$0.30^{+0.09}_{-0.09}$	1.00	6.89 (0.24)	$17.3^{+5.5}_{-4.2}$	11.3 (0.4)	$28^{+9.0}_{-6.9}$
WISP64_210	4.20 (0.34)	$0.33^{+0.07}_{-0.07}$	1.10	7.77 (0.32)	$21.4^{+5.1}_{-4.2}$	12.9 (0.5)	$35^{+8.5}_{-7.0}$
WISP204_133	1.52 (0.25)[c]	$0.00^{+0.00}_{-0.00}$	0.0	3.61 (0.36)	$3.6^{+0.4}_{-0.4}$	6.1 (0.6)	$6.1^{+0.7}_{-0.6}$
WISP27_95	4.17 (0.18)	$0.32^{+0.04}_{-0.04}$	1.07	12.0 (0.2)	$32.0^{+4.2}_{-3.7}$	20.2 (0.4)	$54^{+7.1}_{-6.2}$
WISP147_72	···	···	···	8.27 (0.29)	···	14.0 (0.5)	···
WISP90_58	3.79 (0.16)	$0.24^{+0.04}_{-0.04}$	0.80	15.4 (0.4)	$32.2^{+4.2}_{-3.8}$	26.5 (0.6)	$56^{+7.2}_{-6.6}$
WISP70_253	1.92 (0.11)[c]	$0.00^{+0.00}_{-0.00}$	0.0	3.38 (0.13)	$3.4^{+0.1}_{-0.1}$	5.8 (0.2)	$5.8^{+0.3}_{-0.2}$
WISP175_124	···	···	···	9.53 (0.33)	···	16.5 (0.6)	···
WISP96_158	5.01 (0.93)	$0.48^{+0.16}_{-0.16}$	1.60	6.09 (0.25)	$26.5^{+16.9}_{-10.3}$	10.8 (0.5)	47^{+30}_{-18}
WISP138_160	3.41 (0.39)	$0.15^{+0.10}_{-0.10}$	0.50	13.3 (0.1)	$21.1^{+7.5}_{-5.6}$	24.2 (0.3)	38^{+14}_{-10}
WISP56_210	2.80 (0.64)	$0.00^{+0.16}_{-0.00}$	0.0	10.3 (1.6)	$10.3^{+6.7}_{-1.6}$	19.6 (3.1)	$20^{+12.7}_{-3.2}$
WISP206_261	4.08 (0.31)	$0.30^{+0.06}_{-0.06}$	1.00	5.57 (0.17)	$14.0^{+2.8}_{-2.4}$	10.7 (0.4)	$27^{+5.4}_{-4.5}$

[a] This is the FIRE flux scaled to WFC3 as described in §3.1.1, accounting for the uncertain absolute calibration of the FIRE data. The units are 10^{-17} erg cm^{-2} s^{-1}.
[b] Scaled $F(H\alpha)$ extinction corrected using the $E(B-V)_{gas}$ derived from the Balmer decrement and assuming a Calzetti extinction curve (Calzetti et al. 2000).
[c] Low value likely due to measurement error in Hβ.

where Q_{H^0} is the ionizing photon flux produced by the radiation source(s) and n is the local number density of hydrogen atoms. It is often expressed in terms of the logarithm of the dimensionless ionization parameter U where

$$U \equiv \frac{q}{c} \tag{2}$$

The ionization parameter depends on the nature of the ionizing radiation source(s) as well as the density and geometric distribution of the gas and stars in H II regions. It is useful because it can be measured easily using the ratio of fluxes from different ionization stages of the same element, for example $O32 \equiv$[O III]λ5007/[O II]λ3727.

We used the $O32$ values from the sample together with the IZI code and priors on the metallicity to derive ionization parameter estimates. The extinction-corrected values of $O32$ and inferred log U values are given in Table 4. The ionization parameters for our sample range from $-3.26 < \log U < -1.78$, with a mean log U of -2.59. These values are signficantly elevated with respect to local samples, for which ionization parameters in the range $-4 < \log U < -3$ are typical. The ionization parameters we measure are, however, in close agreement with those measured in other high redshift samples (e.g., Pettini et al. (2001), Hainline et al. (2009), Richard et al. (2011), Wuyts et al. (2012), Nakajima et al. (2013)).

Erb et al. (2010) found a very high ionization parameter of log $U \sim -1$ for the low mass, low metallicity, star-forming galaxy Q2343-BX418 at z=2.3. This galaxy was selected for detailed study based on its low mass and blue UV-continuum slope. While our sample includes galaxies analogous to BX418 in many respects, including stellar mass, metallicity, SFR, half-light radius, and reddening, we do not find any sources with a comparably high ionization parameter. BX418 may be somewhat exceptional in this regard.

4.4. *Star Formation Rates*

The star formation rates for the sample were determined using the extinction-corrected values of $F(H\alpha)$ together with the calibration of Kennicutt (1998) converted to a Chabrier IMF. In this analysis we have assumed that AGN contribution is negligible (this issue is

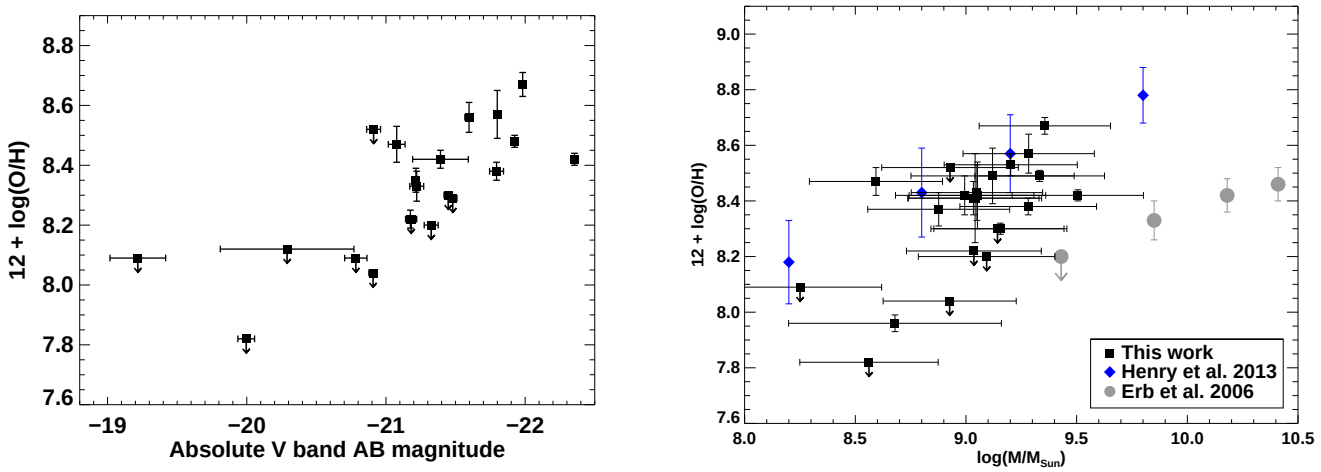

FIG. 6.— *Left:* The $N2$ metallicity vs. absolute magnitude from WFC3 H-band photometry, corresponding to rest-frame optical. The photometry has been corrected for emission line contamination. *Right:* Rough mass estimates from rest-frame optical photometry corrected for emission line flux against the $N2$ metallicity estimates. The blue diamonds are from the recent determination of the MZ relation by Henry et al. (2013) using stacked data from WISP. These values were found using R_{23} so a systematic offset between the two estimates might exist (Kewley & Ellison 2008). Nevertheless, we see relatively good agreement. The gray circles are points determined by Erb et al. (2006). Our points are offset upward from these, which may be due to a combination of a slightly lower average redshift for our sample and possible nitrogen enhancement in the emission-line selected sample, as discussed in §6.3. Such an enhancement could bias our $N2$ metallicities.

TABLE 4
$N2$ AND R_{23} METALLICITY ESTIMATES AND IONIZATION PARAMETERS FOR THE SAMPLE.

Object ID	Z^a ($N2$)	Z^a (R_{23})	$O32$	log U
WISP159_134	< 8.04	···	···	···
WISP134_171	8.35 (0.04)	···	···	···
WISP50_65	···	~ 8.4	-0.46 (0.19)	$-2.98^{+0.07}_{-0.2}$
WISP173_205	···	···	0.71 (0.15)	$-2.20^{+0.63}_{-0.35}$
WISP9_73	8.22 (0.03)	8.44 (0.04)	0.28 (0.19)	$-2.77^{+0.28}_{-0.07}$
WISP43_75	8.57 (0.08)	···	···	···
WISP25_53	8.48 (0.02)	8.81 (0.02)	0.08 (0.25)	$-2.91^{+0.21}_{-0.07}$
WISP46_75	8.42 (0.03)	8.87 (0.09)	-0.34 (0.26)	$-3.26^{+0.21}_{-0.07}$
WISP126_90	8.67 (0.04)	···	···	···
WISP22_111	8.56 (0.05)	···	···	···
WISP22_216	< 7.82	···	···	···
WISP64_2056	< 8.09	···	···	···
WISP81_83	···	···	···	···
WISP138_173	< 8.20	~ 8.4	-0.14 (0.21)	$-2.76^{+0.14}_{-0.14}$
WISP170_106	< 8.30	~ 8.4	0.22 (0.25)	$-2.76^{+0.21}_{-0.14}$
WISP64_210	8.47 (0.06)	~ 8.4	0.47 (0.06)	$-2.41^{+0.14}_{-0.28}$
WISP204_133	< 8.52	8.00 (0.11)	0.12 (0.15)	$-2.91^{+0.28}_{-0.07}$
WISP27_95	8.38 (0.03)	~ 8.4	0.08 (0.15)	$-2.93^{+0.21}_{-0.07}$
WISP147_72	···	···	0.78 (0.30)	$-2.06^{+0.80}_{-0.49}$
WISP90_58	8.42 (0.02)	8.62 (0.03)	0.08 (0.25)	$-2.93^{+0.28}_{-0.09}$
WISP70_253	< 8.12	7.96 (0.03)	0.86 (0.07)	$-1.88^{+0.40}_{-0.53}$
WISP175_124	8.33 (0.05)	···	0.46 (0.05)	$-2.62^{+0.35}_{-0.07}$
WISP96_158	< 8.22	~ 8.4	0.41 (0.13)	$-2.55^{+0.28}_{-0.21}$
WISP138_160	8.29 (0.02)	···	···	···
WISP56_210	···	~ 8.4	0.61 (0.06)	$-1.78^{+0.73}_{-0.60}$
WISP206_261	< 8.09	8.37 (0.06)	0.69 (0.13)	$-2.34^{+0.56}_{-0.21}$

[a] In units of 12+log(O/H).

discussed further in §6.1). The results are summarized in Table 3. The estimated star formation rates range from $\sim 5-100$ $M_\odot$ yr^{-1} with an average of 29 $M_\odot$ yr^{-1} and a median of 27 $M_\odot$ yr^{-1}. As noted previously, the sources with the highest extinction-corrected SFRs tend to be those sources with more dust extinction overall, but this could be a selection effect.

4.5. *Line Widths & Dynamical Mass Estimates*

The emission line velocity dispersions are resolved in the FIRE spectra and are summarized in Table 5. Figure 7 shows a histogram of the measured dispersions (deconvolved with the instrumental resolution), which range from 50 to 200 km s^{-1}, but show a peak around $\sim$70 km s^{-1}. These dispersions are comparable to those found for the sample of Lyman-break galaxies at $z \sim 3$ analyzed in Pettini et al. (2001).

Comparable (though generally more massive) star-forming galaxies at $z \sim 2$ have been shown through integral field studies (e.g. Law et al. 2009, Genzel et al. 2011) to have gas kinematics that are often dominated by turbulent motions with large intrinsic velocity dispersions. For any particular galaxy it is difficult to know if the line width results from rotation-dominated galaxy dynamics, turbulent motions of gas within regions of high star formation surface density, or some combination of these. Two galaxies in our sample (WISP43_75 and WISP25_53) show evidence for rotational motion in the FIRE 2D spectra, but the majority show no clear spatial gradient in the 2D emission lines. One source, WISP81_83, shows double-peaked emission lines separated by 290 km s^{-1}, likely due to either a small merger in progress or an unresolved disk. WISP43_75 also shows what appears to be two-component emission in Hα, though less pronounced than WISP81_83.

Following the analysis of Maseda et al. (2013) and references therein, we can estimate the dynamical mass of galaxies in the sample using the emission line velocity

dispersions and half-light radii from the formula

$$M_{dyn} = C\frac{r_{\rm eff}\sigma^2}{G} \quad (3)$$

The constant C is a geometric correction factor that can vary depending on the assumed shape and orientation of the galaxies. We adopt $C = 3$ as in Maseda et al., with a quoted uncertainty of 33%. The half-light radii are measured from the direct H-band images from WFC3, and are summarized in Table 5. In Figure 8 we plot the dynamical masses obtained in this way against the rough stellar mass estimates obtained as described in §4.2.

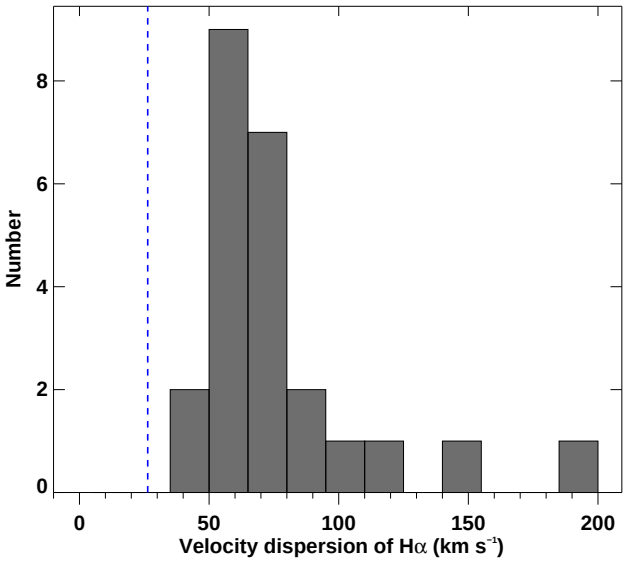

FIG. 7.— The velocity dispersions of the Hα lines. The blue dashed line shows the average resolution of FIRE (62 km s^{-1} FWHM = 26.4 km s^{-1} in sigma). The line velocity dispersions have been deconvolved with the instrumental resolution.

The dynamical mass estimates from Equation 3 are plotted as upper limits, because the line dispersions are a result of both rotational and turbulent/thermal motions of the gas and the relative contribution of these is uncertain. Our dynamical and stellar mass estimates show a strong correlation and are in relatively good agreement with the 0.57 dex offset found by Maseda et al. between the two estimates. This offset indicates that stars contribute ∼27% to the mass, assuming all of the dispersion is dynamical in origin. However, random motions of the gas may contribute substantially to the line dispersions, which would in part explain the offset between the dynamical and stellar mass estimates.

4.6. *Morphologies*

While detailed morphological modeling of the galaxies is beyond the scope of this paper, we may make some observations based on visual inspection of the WFC3 imaging data. The H-band imaging (corresponding to rest-frame optical) for the galaxies in the sample reveals that a large fraction ($\gtrsim$40%) show evidence for disruption or asymmetry, probably indicative of merging or the existence of multiple star-forming clumps. Additionally, most sources are quite compact, with measured half-light radii typically $\lesssim$ 2.5 kpc.

An interesting example of a probable merger-driven starbursting galaxy is WISP96_158, which lies in one of the deepest WISP pointings. A serendipitous detection of [O III] emission in the FIRE 2D spectrum from a neigh-

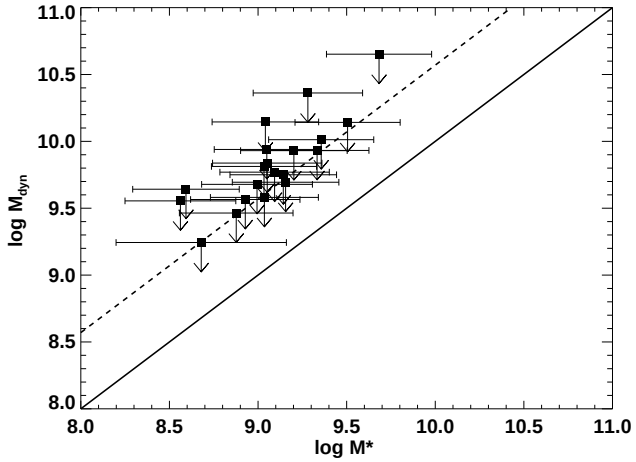

FIG. 8.— The dynamical mass estimated from Equation 3 (in units of $M_\odot$) against the stellar mass estimates from the WFC3 photometry. The dynamical mass estimates (plotted as upper limits) are systematically higher by ∼0.6 dex, which may reflect a low ($\sim$ 30%) contribution of stars to the dynamical masses of the systems. However, the dynamical mass estimates are also likely to be elevated by random/turbulent motions of the gas affecting the measured line dispersions.

TABLE 5
VELOCITY DISPERSIONS AND HALF-LIGHT RADII FOR THE SAMPLE.

Object ID	σ([O III]) (km s^{-1})	σ(Hα) (km s^{-1})	R_e (kpc)
WISP159_134	45.7 (3.0)	64.9 (4.3)	···
WISP134_171	111.8 (5.2)	71.5 (2.1)	2.4
WISP50_65	152.4 (20.0)	145.5 (3.8)	2.7
WISP173_205	65.4 (1.3)	61.3 (1.4)	1.5
WISP9_73	85.9 (2.6)	79.0 (1.0)	1.5
WISP43_75	···	···	3.2
WISP25_53	74.5 (0.8)	75.9 (1.2)	2.2
WISP46_75	66.1 (10.4)	69.4 (3.9)	···
WISP126_90	···	78.1 (1.5)	2.4
WISP22_111	80.2 (12.5)	68.3 (1.9)	2.6
WISP22_216	40.9 (1.7)	48.2 (1.7)	2.2
WISP64_2056	52.8 (1.0)	58.5 (1.9)	···
WISP81_83	···	···	2.8
WISP138_173	62.3 (2.7)	60.5 (6.4)	2.2
WISP170_106	71.4 (4.0)	55.2 (3.2)	1.6
WISP64_210	64.8 (1.5)	74.5 (4.7)	1.6
WISP204_133	55.3 (8.4)	54.9 (11.2)	1.7
WISP27_95	128.4 (1.3)	109.6 (3.0)	2.0
WISP147_72	202.4 (1.3)	186.7 (7.2)	1.6
WISP90_58	110.4 (1.9)	111.9 (2.9)	1.6
WISP70_253	39.6 (0.7)	51.2 (3.2)	1.6
WISP175_124	71.1 (1.0)	85.1 (4.5)	2.0
WISP96_158	47.5 (1.5)	50.7 (3.2)	2.4
WISP138_160	66.0 (0.4)	56.5 (0.8)	1.6
WISP56_210	97.7 (5.7)	84.0 (23.3)	2.1
WISP206_261	46.5 (0.8)	39.4 (1.7)	1.9

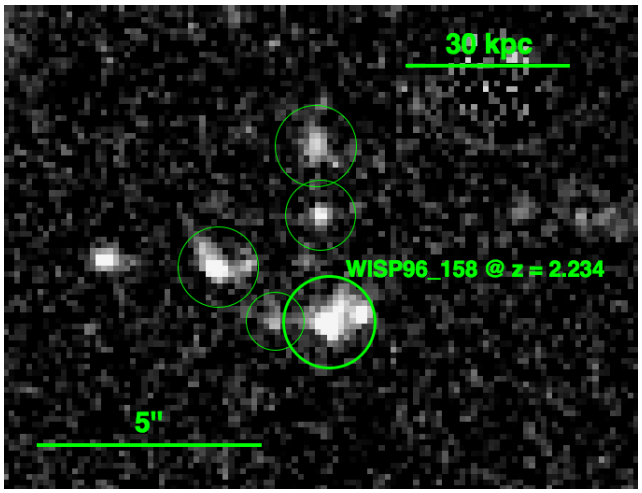

FIG. 9.— The emission-line galaxy WISP96_158 lies in one of the deepest WISP fields (28081 sec and 11430 sec exposures in the G102 and G141 grisms, respectively, and a 4295 sec direct image in the F110W filter, shown). A serendipitous detection of [O III]λ5007 in the FIRE 2D spectrum from a neighboring galaxy led to the identification of the small group of galaxies (circled) at the same redshift as WISP96_158. A significant fraction of strong emission-line galaxies at $z \sim 2$ are plausibly triggered by small gas-rich mergers in systems such as this one.

boring galaxy led to the identification of a small group of objects at the same redshift as the main emission-line galaxy. In Figure 9 we show the unusually deep WISP F110W exposure, in which we can clearly see the system of small galaxies surrounding WISP96_158, which itself appears clumpy and disturbed. It seems likely that this starburst is triggered by the interaction/merger of small systems.

5. COMPOSITE OPTICAL SPECTRUM

We constructed a composite 1D spectrum using the FIRE spectra, in order to probe the average properties of emission-line galaxies at $z \sim 2$ in greater detail. The composite contains 24 sources from FIRE, with two sources, WISP81_83 and WISP43_75, excluded due to the presence of multiple velocity components in their emission lines. To create the composite we shifted the individual 1D spectra to rest frame, interpolated to a common dispersion of 0.2 Å, and performed an inverse-variance weighted average of the flux at each wavelength after scaling the spectra to a common $F(\mathrm{H}\alpha)$. The weighting was done to minimize the contribution of OH line residuals from individual spectra. To verify that the result is not driven by a handful of individual spectra, we also performed a median combine and an unweighted average, both of which gave nearly identical results.

The composite 1D spectrum is shown in Figure 10. In Table 6 we give the emission line fluxes for the composite, normalized to $F(\mathrm{H}\beta)$=1.

5.1. *Average Physical Properties from the Composite Spectrum*

The physical properties of the composite are summarized in Table 7. The composite spectrum has a low extinction of $E(B-V) = 0.08 \pm 0.01$ as derived from its Balmer decrement of $\mathrm{H}\alpha/\mathrm{H}\beta = 3.17$. We computed the metallicity of the composite using the $N2$ and R_{23} (upper and lower branch) calibrations, as well as with the interpolation code IZI. The metallicity estimates are in relatively good agreement and yield a similar metallicity ($\sim$0.50 $Z_\odot$) as found on average from the individual spectra. The ionization parameter for the composite is $\log U \sim -2.49$, which is also consistent with the estimates from the individual FIRE spectra.

The velocity dispersion in Hα for the composite spectrum is 78 km s^{-1}. This value is in agreement with the $\langle\sigma_{mean}\rangle = 78 \pm 17$ km s^{-1} found for the similar sample analyzed by Law et al. (2009) at $z \sim 2$, which comprised 12 star-forming galaxies selected to have well-detected Hα or [O III] emission.

5.1.1. *Limit on T_e from the Composite*

The ratio of [O III]λ4959, 5007 to [O III]λ4363 is a direct temperature indicator as it probes the relative abundance of electrons with the different excitation energies needed to produce these lines. [O III]λ4363 is not detected in the composite, but we are able to put a limit on its value: $F([\mathrm{O\ III}]\lambda4363) < 0.11$ (2σ) on a scale in which $F(\mathrm{H}\beta)$=1. This gives an upper limit of $T_e < 16,800$ K on the average gas temperature (Osterbrock & Ferland 2006).

5.1.2. *Electron Density from [S II] and [O II]*

Electron densities can be estimated from the collisionally excited forbidden lines [S II]λ6716, 6731 and [O II]λ3726, 3729, both of which are cleanly detected in the FIRE composite spectrum. We measure [S II]$\lambda6716/\lambda6731 = 1.29 \pm 0.07$ and [O II]$\lambda3729/\lambda3726 = 1.16 \pm 0.13$. These values are both consistent with $n_e \simeq 100 - 400$ cm^{-3}. This density range is elevated in comparison with typical H II regions in the local universe, which generally have $n_e \sim$50–100 cm^{-3} (Brinchmann et al. 2008b; Shirazi et al. 2013).

Shirazi et al. (2013) argued that the elevated ionization parameters observed in high redshift star-forming galaxies are a result of higher electron densities, on the order of $\sim 10^3$ cm^{-3}. The higher average densities we find are consistent with this being a factor driving the higher ionization parameters at high redshift. However, ionization parameter scales weakly with electron density: $U \propto n_e^{1/3}$ (Charlot & Longhetti 2001), and the $\sim$4$\times$ higher electron density we find with respect to local samples is, therefore, probably not the only cause of the $\sim$0.5-1.0 dex higher ionization parameters in the high redshift emission-line galaxies. The volume-averaged rate of production of ionizing photons in these galaxies, which have concentrated, low metallicity star formation, may be another major factor producing the high ionization parameters.

6. ANALYSIS

6.1. *BPT Diagram and AGN Contribution*

Baldwin, Phillips & Terlevich (BPT) diagrams (Baldwin et al. 1981) use emission line ratios to distinguish star-forming galaxies from AGN. We were able to measure the four lines required for the [O III]/Hβ vs. [N II]/Hα BPT diagnostic for nine galaxies in our sample, and eight more for which a meaningful limit on F([N II]) could be placed. The resulting BPT plot is shown on the left panel of Figure 11. Galaxies that are not shown had

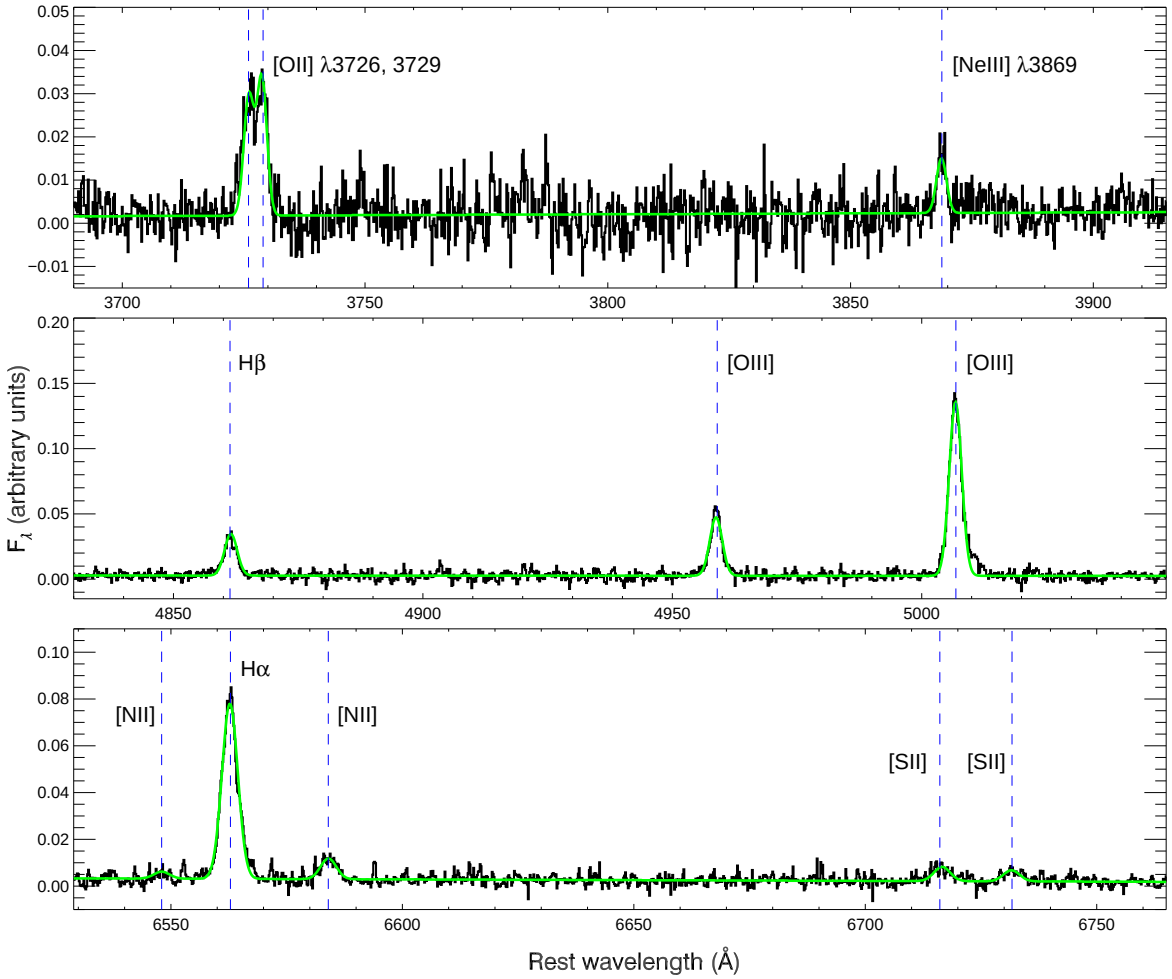

FIG. 10.— The composite FIRE spectrum of 24 emission-line galaxies from the WISP survey, with an average redshift of $\langle z \rangle = 1.85 \pm 0.39$. The fit is overlaid in green.

TABLE 6
LINE FLUX MEASUREMENTS FROM COMPOSITE SPECTRUM, NORMALIZED SUCH THAT $F(\mathrm{H}\beta)$=1.

Line	Value
F([OII]λ3726)	0.702 (0.064)
F([OII]λ3729)	0.815 (0.057)
F([NeIII]λ3869)	0.324 (0.017)
F([Hβ])	1.000 (0.008)
F([OIII]λ5007)	4.116 (0.007)
F([Hα])	3.170 (0.013)
F([NII]λ6583)	0.372 (0.010)
F([SII]λ6716)	0.264 (0.010)
F([SII]λ6731)	0.205 (0.009)

TABLE 7
PHYSICAL PARAMETERS DERIVED FROM THE COMPOSITE SPECTRUM.

Parameter	Value
$\sigma_{(\mathrm{H}\alpha)}$	78 km s^{-1}
$\sigma_{([\mathrm{OIII}])}$	75 km s^{-1}
Hα/Hβ	3.17 (0.03)
$E(B-V)_{\mathrm{nebular}}$	0.08 (0.01)
12+log(O/H) ($N2$)	8.37 (0.01)
12+log(O/H) ($R23$, lower)	8.20 (0.01)
12+log(O/H) ($R23$, upper)	8.68 (0.01)
12+log(O/H) (IZI)	8.46 (0.08)
$O32$[a]	0.39 (0.05)
log U	-2.49$^{+0.07}_{-0.14}$

[a] Corrected for dust extinction using Balmer decrement.

one or more of the relevant emission lines contaminated by an OH sky line.

The position occupied by the overall composite spectrum is shown as a black filled square. Additionally, we generated composite spectra at $z \sim 1.5$ and $z \sim 2.2$ using the procedure described in the previous section and measured the diagnostic ratios from them in order to search for possible evolution over this redshift interval. It should be noted that all of these composites contain additional objects that we were not able to include individually in the plot.

A clear feature of this plot is the average upward offset of [O III]/Hβ for a given [N II]/Hα of the $z \sim 2$ sample relative to local star-forming galaxies. This trend has been

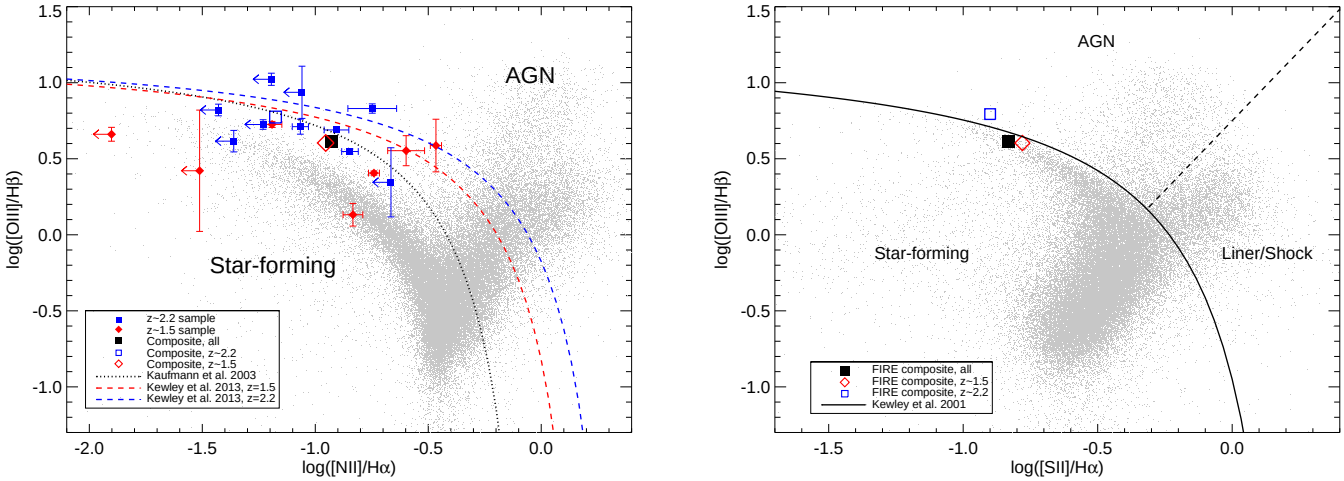

FIG. 11.— *Left:* The BPT diagram for the galaxies in the sample for which we could measure the required lines. The small gray points are 60,000 sources from SDSS for comparison. Upper limits on log([N II]/Hα) at the 95% confidence level are given for those sources for which [N II]λ6583 was not detected. The black square and open symbols are the result for the composite FIRE 1D spectra (note that the error bars for these are smaller than the symbols). The [O III]/Hβ ratio for our sources is systematically higher than for star-forming galaxies in the local universe, a trend that has been noted previously. We show the empirical maximum starburst line from Kauffmann et al. (2003). Recently, Kewley et al. (2013b) proposed a redshift-dependent formulation of the starburst/AGN dividing line, shown here for $z = 1.5$ and $z = 2.2$. The majority of our points are consistent with being highly star-forming galaxies according to these demarcations. *Right:* The BPT diagnostic diagram using the ratio [SII]/Hα in place of [NII]/Hα (Veilleux & Osterbrock 1987). Our composite spectrum from FIRE falls along the metal-poor tail of the local star-forming sequence from SDSS. No evidence for significant AGN or LINER/shock contribution to the emission lines is evident from this diagnostic.

noted in previous studies (Shapley et al. 2005; Erb et al. 2006; Liu et al. 2008; Hainline et al. 2009; Newman et al. 2013), and has been linked to higher ionization parameters, on average, in star-forming galaxies at high redshift (e.g. Brinchmann et al. 2008b; Kewley et al. 2013b). The one galaxy in the sample that does fall on the local star-forming sequence in this diagram, WISP46_75, also has the lowest measured ionization parameter.

Recently Kewley et al. (2013b) presented a redshift-dependent parameterization of the AGN/starburst boundary line, motivated by the observational evidence for systematic offsets in the diagram for galaxies at high redshift. These lines are plotted on the left panel of Figure 11 for $z = 2.2$ and $z = 1.5$. It can be seen both from the individual galaxies and the composites that the sources at $z \sim 2.2$ tend to have higher [O III]/Hβ ratios in comparison with those at $z \sim 1.5$. The composite spectra are in fact consistent with being "maximal starbursts" according to the empirical demarcation of Kauffmann et al. (2003), while falling well above the locus of star-forming galaxies in the local universe. The $z \sim 2.2$ composite is offset to the upper left of the $z \sim 1.5$ composite, hinting at an evolutionary trend over this redshift interval. However, this may be (at least in part) due to a selection effect resulting from the fact that the $z \sim 2.2$ sample was selected on the basis of [O III] emission, while the $z \sim 1.5$ sample was often selected on the basis of Hα emission without regard to the strength of [O III].

We plot the positions of the FIRE composite spectra on the log([O III]/Hβ) versus log([S II]/Hα) diagnostic (Veilleux & Osterbrock 1987) on the right panel of Figure 11. The $z \sim 2.2$ composite is again offset to the upper left from the $z \sim 1.5$ composite. Notably, there is no obvious offset of the overall composite spectrum in this diagram with respect to the local, metal-poor star-forming sequence from SDSS.

The elevated [O III]/Hβ ratios in the classical BPT diagram could be at least partially due to AGN activity in such galaxies (Trump et al. 2011, 2013; Kewley et al. 2013a). While a few objects in our sample fall close to the composite region of the BPT diagram, most are consistent with a purely star-forming classification. The positions of the composite spectra in the BPT diagrams, in particular, argue against signficant AGN contribution. Nevertheless, caution is required in interpreting these diagrams at high redshift. For example, Kewley et al. (2013a) showed that the effect of a low-metallicity AGN on the [O III]/Hβ versus [N II]/Hα diagram can be indistinguishable from the offset caused by more extreme star-forming conditions. However, the position of the composites on the [O III]/Hβ versus [S II]/Hα diagram, as well as the relatively low ($\sim$75 km s^{-1}) average velocity dispersion of the emission lines, also disfavor significant AGN contribution. We conclude that AGN activity in high-EW emission-line galaxies at $z \sim 2$ is likely to be minimal.

6.2. *High [O III]/Hα and [O III]/Hβ Ratios*

A significant fraction of galaxies in the our sample show quite high [O III]λ5007 emission relative to the recombination lines Hα and Hβ. Both Domínguez et al. (2013) and Colbert et al. (2013) also noted the relatively large number of sources in the WISP survey with high [O III]/Hα ratios and found a negative correlation between the ratio [O III]/Hα and Hα luminosity. High [O III]/Hβ ratios were also found to be characteristic of Lyman-break selected galaxies at $z \sim 3.5$ by Holden et al. (2014).

The [O III]/(Hα,Hβ) line ratios we find for a number of galaxies in our sample are higher than the maximum values predicted by photoionization model grids for low-metallicity galaxies (e.g. Levesque et al. 2010).

TABLE 8
Comparison of the properties of composite spectra binned by the ratio [O III]/Hα.

Parameter	[O III]/Hα > 1.55	[O III]/Hα < 1.55
12+log(O/H) ($N2$)	8.22 (0.04)	8.34 (0.03)
12+log(O/H) (Model grid)	8.30 (0.03)	8.46 (0.10)
O3O2	0.59 (0.05)	0.26 (0.09)
Ne3O2	-0.52 (0.09)	-0.74 (0.08)
log U	-2.1 (0.2)	-2.6 (0.2)
[S II]λ6716/[S II]λ6731	1.28 (0.32)	1.34 (0.18)
[O II]λ3729/[O II]λ3726	1.09 (0.33)	0.95 (0.35)

The $O32$ ratios for these sources indicate high ionization parameters, but not high enough to account for the [O III]/(Hα,Hβ) ratios. To investigate this further we made composite FIRE spectra of subsamples with high and low [O III]/Hα ratios, with the dividing ratio being [O III]/Hα=1.55 to give a roughly equal number of galaxies in each composite. The physical parameters derived from these composite spectra are summarized in Table 8. A few things emerge from these composites:

1. The cut on the ratio [O III]/Hα largely splits in a similar way as the cut on redshift, with high [O III]/Hα ratios more common among the $z \sim 2.2$ sample. As mentioned previously, this could be a selection effect given that the $z \sim 2.2$ sample was selected based on [O III] emission.

2. The [N II]/Hα ratio is lower for the composite of galaxies with high [O III]/Hα, most likely indicative of lower metallicity for those sources, although a higher ionization parameter can also lower this ratio. The correlation of [O III]/Hα and metallicity has been noted previously (Liang et al. 2006; Colbert et al. 2013), and is related to the shape of the star-forming sequence in the BPT diagram.

3. The sources with higher [O III]/Hα have significantly stronger [Ne III]/[O II] and [O III]/[O II] ratios than those with lower [O III]/Hα. Both of these ratios are sensitive to ionization parameter (Levesque & Richardson 2013), suggesting (as expected) that the higher ionization parameter is a key factor in elevating the [O III]/Hα ratio.

4. Roughly the same electron density is inferred for both composites from the density-sensitive doublets [O II]λ3726,3729 and [S II]λ6716,6731, although there is considerable uncertainty in the measurements.

Overall, what we infer from this comparison is that the sources with elevated [O III]/Hα and [O III]/Hβ ratios have higher ionization parameters, as expected, but that the difference seems more linked to their lower metallicity than a difference in electron density. The relationship between ionization parameter and metallicity is also known to exist for local star-forming galaxies (Dopita et al. 2000; Kewley & Dopita 2002). Metallicity influences ionization parameter through its effect on stellar radiation: at low metallicity the UV flux from metal-poor stars is more intense due to decreased metal-line blanketing in stellar atmospheres. Moreover, rotational mixing in massive, rotating stars can lead to more efficient mass loss and facilitate the onset of the Wolf-Rayet phase and a corresponding hardening of the spectrum; this effect is predicted be more pronounced in low-metallicity environments (Leitherer 2008; Levesque et al. 2012; Kewley et al. 2013a). While electron density does not differentiate the two composites, both have higher electron densities than local samples.

6.3. *What drives the BPT diagram offset?*

The upward offset of many high redshift star-forming galaxies in the [O III]/Hβ versus [N II]/Hα diagram relative to the local star-forming sequence has been interpreted as resulting from more extreme star forming conditions in the early universe. Brinchmann et al. (2008b) showed that the offset from the ridgeline in the BPT diagram correlates closely with EW(Hα) in SDSS, and from this inferred that higher ionization parameter (which likely is related to EW(Hα)) is behind the effect.

The galaxies in our sample do have elevated ionization parameters relative to local samples, and show the offset in the [O III]/Hβ versus [N II]/Hα diagram seen in other high redshift star-forming galaxies. However, the composite spectrum from the FIRE sample does not show an analogous offset from the local metal-poor star-forming sequence in the [O III]/Hβ versus [S II]/Hα diagram, which is somewhat puzzling if more extreme star-forming conditions are the root of the offset in the [O III]/Hβ versus [N II]/Hα diagram. Moreover, the ionization parameters we measure for the sample, corresonding to log q values of $\sim$7.5-8.5, are simulated in up-to-date photoionization models (e.g., Dopita et al. 2013), and generally do not produce as large of an offset in the [O III]/Hβ versus [N II]/Hα diagram as what is observed.

Thus it is worth considering alternative explanations for the offset of high redshift star-forming galaxies from the local star-forming sequence in the [O III]/Hβ versus [N II]/Hα diagram. One possible cause of such an offset is a higher average nitrogen-to-oxygen abundance ratio (Pérez-Montero & Contini 2009). The N/O ratio for galaxies is roughly flat (though with significant scatter) at low metallicities, with a plateau value of log(N/O) ~ -1.5, and increases at higher metallicities due to the secondary production of nitrogen through the CNO cycle (Henry et al. 2000). Cases of enhanced nitrogen abundance have been found in starburst galaxies in the local universe. For example, the blue compact starburst galaxy NGC 5253 is known to have regions of 3$\times$ higher nitrogen abundance than normally found in metal-poor galaxies (Welch 1970; Walsh & Roy 1987; Kobulnicky et al. 1997), which seem to be associated with super star clusters (Westmoquette et al. 2013). Andrews & Martini (2013), using stacked spectra from SDSS, found that the log(N/O) ratio tends to be higher at a given metallicity for galaxies with higher SFRs. Additionally, Amorín et al. (2010) presented evidence that the so-called "green pea" galaxies found in SDSS (which, with strong [O III] emission lines and compact sizes, may be low-redshift analogues of the galaxies in our $z \sim 2$ sample) show systematically high log(N/O) values for their metallicities.

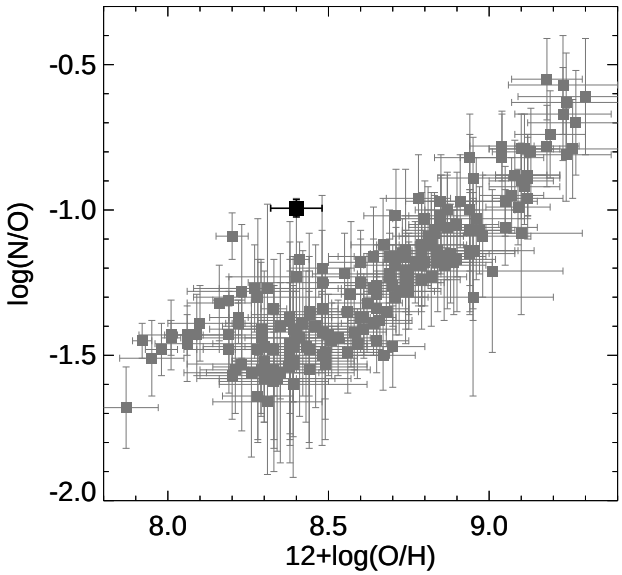

FIG. 12.— The nitrogen-to-oxygen abundance ratio vs. metallicity computed from the FIRE composite spectrum (black square) compared with values from local H II regions (van Zee et al. 1998).

To investigate this possibility, we used the calibration of Thurston et al. (1996), based on the dust-corrected ratio $\log(N^+/O^+)$, to compute the value of log(N/O) for the composite FIRE spectrum. We adopted a nebular temperature of 10,000 K, yielding a value of $\log(N/O) = -0.99 \pm 0.03$. For higher nebular temperatures log(N/O) increases, so we consider this to be a relatively conservative lower limit††. We also computed log(N/O) using the ratio N2S2 = log([N II]/[S II]) as in Amorín et al. (2010), yielding $\log(N/O) = -0.94 \pm 0.05$. Comparing these results to the measured log(N/O) values as a function of 12+log(O/H) in the literature (van Zee et al. 1998; Liang et al. 2006; van Zee & Haynes 2006; Berg et al. 2012; Andrews & Martini 2013), we find that the log(N/O) of the FIRE composite is higher by approximately 0.4 dex than the average value for galaxies at similar metallicity locally. The offset is illustrated in Figure 12, in which we show the FIRE composite spectrum in comparison with the data from local H II regions from van Zee et al. (1998).

From this analysis, it seems plausible that the offset of star-forming galaxies at high redshift in the [O III]/Hβ versus [N II]/Hα diagram is, to some extent, an offset in [N II]/Hα caused by systematically high N/O ratios. We now consider why this might be the case.

One mechanism for producing a nitrogen enhancement is through the inflow of metal-poor gas. Inflows can lower the metallicity (O/H) of a galaxy with a high N/O abundance ratio (from secondary nitrogen production) while preserving the high N/O ratio (van Zee et al. 1998; Köppen & Hensler 2005). We consider this unlikely to be the explanation of enhanced N/O in emission-line galaxies at $z \sim 2$, which are relatively young and metal-poor, and thus would not have had time to enter the secondary nitrogen production regime.

A more likely cause of the nitrogen enhancement, in our view, is a significant population of Wolf-Rayet (W-R) stars in the $z \sim 2$ emission-line galaxies. The connection between nitrogen-enriched galaxies and the influence of W-R stars has been known for some time (Pagel et al. 1986; Henry et al. 2000), and recent evidence has been found that low-redshift galaxies with W-R features in their optical spectra often display enhanced nitrogen abundances (Brinchmann et al. 2008a; López-Sánchez & Esteban 2010; Berg et al. 2011). However, the effect is generally smaller than the enhancement we find in the $z \sim 2$ sample.

Kobulnicky et al. (1997) suggested that the significantly nitrogen-enhanced regions of NGC 5253 (comparable to the enhancement we see in the $z \sim 2$ sample) result from the winds of W-R and/or related luminous blue variable (LBV) stars. Westmoquette et al. (2013) argued that the hot winds of these stars are able to mix with the cooler surrounding ISM because of the unusually high pressure environment the stars inhabit. This explanation may hold for the high redshift emission-line galaxies as well, which have higher nebular gas densities than local galaxies and probably harbor very dense star clusters to produce the observed emission lines.

A potential problem with this explanation is that the fraction of massive stars entering the W-R phase should decline with metallicity, so one would expect that the ratio of W-R to O stars would be lower in galaxies at high redshift. However, the metallicity of NGC 5253, $12 + \log(O/H) \sim 8.3$, is comparable to that of the galaxies in our emission-line sample at $z \sim 2$, and Brinchmann et al. (2008a) also find a large number of low-metallicity galaxies with W-R features. Moreover, the ratio of nitrogen- (WN) to carbon (WC)-sequence W-R stars increases strongly at lower metallicities (Crowther 2007), and WN-sequence stars would be most responsible for ejecting nitrogen into the ISM, leading to the observed enhancement.

It should be noted that evidence already exists for significant numbers of W-R stars in star-forming galaxies at high redshift. The composite rest-frame UV spectrum of $z \sim 3$ Lyman-break galaxies presented in Shapley et al. (2003) shows relatively strong and broad He II λ1640 emission, as does the rest-frame UV spectrum obtained by Erb et al. (2010) for the low-metallicity galaxy BX418 at $z = 2.3$. This feature is attributed to the fast, dense winds of W-R stars. As discussed by those authors, reproducing the He II λ1640 emission is difficult with existing stellar population synthesis models. In order to do so, very young starburst ages, a top-heavy initial mass function (IMF), or physical effects due to binary stellar evolution must be invoked. Clearly, there is still much that is not fully understood about the star formation in these environments.

7. SUMMARY & DISCUSSION

We have presented rest-frame optical spectra taken with Magellan FIRE of a sample of 26 emission-line galaxies at $z \sim 1.5$ and $z \sim 2.2$ selected from the HST-WFC3 grism spectroscopy of the WISP survey. The FIRE spectra provide significant additional information

††If, rather than use the calibration of Thurston et al. (1996), we assume that $\log(N/O) \simeq \log(N^+/O^+)$ (as is often done in the literature), we obtain a higher value: $\log(N/O) = -0.60 \pm 0.06$.

about these galaxies, allowing us to measure metal abundances, dust reddening, kinematics, star formation rates and important diagnostic line ratios. We also created composite spectra that reveal further details about the average properties of the sample.

Direct WFC3 imaging shows the sources to be compact, with many ($\gtrsim$40%) exhibiting clumpiness or asymmetry. The galaxies are low mass ($\sim10^{8.5}$–$10^{9.5}$ $M_\odot$), with a median metallicity of 0.45 $Z_\odot$. A clear mass-metallicity relation is found for the sample. As seen in other high-redshift samples, the ionization parameters of the galaxies in our sample are significantly higher, on average, than those found for typical star-forming galaxies in the local universe. The velocity dispersions of the emission lines for the sample range from $\sim$50–200 km s^{-1} but usually are around 75 km s^{-1}. Assuming that the dispersions are almost entirely due to gravitational motions (which is probably not the case), this implies that stars make up roughly 30% of the dynamical mass of the galaxies.

The composite spectra we generated from the FIRE sample reveal more detail about the average properties of emission-line galaxies at $z \sim 2.2$ and $z \sim 1.5$. From the overall composite we infer an average electron density for the star-forming regions of 100-400 cm^{-3} and put a limit on the average temperature in these regions of $T_e < 16,800$ K from the non-detection of [O III]λ4363. The locations of galaxies and composites on the BPT diagnostic diagrams favor a starburst classification, and we find little evidence for substantial AGN contribution.

Our sample includes galaxies with unusually high [O III]/Hα and [O III]/Hβ line ratios that are not reproduced with existing photoionization models. Composite spectra sorted on the ratio [O III]/Hα indicate that those sources with high [O III]/Hα ratios show stronger [O III]λ5007 and [Ne III]λ3869 emission relative [O II]λ3727, indicating higher ionization parameters. The high [O III]/(Hα,Hβ) sources tend to be lower metallicity, which seems to be the main factor driving their higher ionization parameters. Reproducing the line ratios observed in such objects may require modifications to photoionization models to better account for the star-forming conditions in high redshift galaxies.

The well-known offset of high redshift star-forming galaxies from the local star-forming sequence in the [O III]/Hβ versus [N II]/Hα diagnostic diagram is observed in our sample, but we do not find a similar offset in the [O III]/Hβ versus [S II]/Hα diagram. We therefore investigated the possibility that the offset of high-redshift galaxies in the [O III]/Hβ versus [N II]/Hα diagram may result, at least in part, from elevated nitrogen abundances. The composite FIRE spectrum was used to infer the N/O abundance ratio, which we find to be $\sim$0.4 dex higher in comparison with local galaxies of similar metallicity. We speculate that an elevated nitrogen abundance in high redshift star-forming galaxies may be common, and could be explained by the presence of a substantial population of Wolf-Rayet stars embedded in super star clusters in such galaxies.

We thank the anonymous referee for thoughtful comments and suggestions that significantly improved this paper, and Evan Skillman for a careful reading and helpful comments. We are also grateful to Rob Simcoe, Lisa Kewley, Ryan Quadri, Daniel Kelson and Louis Abramson for discussions regarding the FIRE observations and science. DCM gratefully acknowledges the support provided by the Carnegie Observatories graduate research fellowship, as well as the excellent support provided by the staff of the Las Campanas Observatory. CLM acknowledges support from NSF AAG 1109288.

REFERENCES

Abazajian, K. N., Adelman-McCarthy, J. K., Agüeros, M. A., et al. 2009, ApJS, 182, 543
Amorín, R. O., Pérez-Montero, E., & Vílchez, J. M. 2010, ApJ, 715, L128
Andrews, B. H., & Martini, P. 2013, ApJ, 765, 140
Asplund, M., Grevesse, N., Sauval, A. J., & Scott, P. 2009, ARA&A, 47, 481
Atek, H., Malkan, M., McCarthy, P., et al. 2010, ApJ, 723, 104
Atek, H., Siana, B., Scarlata, C., et al. 2011, ApJ, 743, 121
Baldwin, J. A., Phillips, M. M., & Terlevich, R. 1981, PASP, 93, 5
Belli, S., Jones, T., Ellis, R. S., & Richard, J. 2013, ArXiv e-prints
Berg, D. A., Skillman, E. D., & Marble, A. R. 2011, ApJ, 738, 2
Berg, D. A., Skillman, E. D., Marble, A. R., et al. 2012, ApJ, 754, 98
Brammer, G. B., Sanchez-Janssen, R., Labbe, I., et al. 2012, ArXiv e-prints
Brinchmann, J., Kunth, D., & Durret, F. 2008a, A&A, 485, 657
Brinchmann, J., Pettini, M., & Charlot, S. 2008b, MNRAS, 385, 769
Bruzual, G., & Charlot, S. 2003, MNRAS, 344, 1000
Calzetti, D., Armus, L., Bohlin, R. C., et al. 2000, ApJ, 533, 682
Charlot, S., & Longhetti, M. 2001, MNRAS, 323, 887
Colbert, J. W., Teplitz, H., Atek, H., et al. 2013, ArXiv e-prints
Cowie, L. L., Barger, A. J., & Hu, E. M. 2011, ApJ, 738, 136
Crowther, P. A. 2007, ARA&A, 45, 177
Daddi, E., Cimatti, A., Renzini, A., et al. 2004, ApJ, 617, 746
Domínguez, A., Siana, B., Henry, A. L., et al. 2013, ApJ, 763, 145
Dopita, M. A., Kewley, L. J., Heisler, C. A., & Sutherland, R. S. 2000, ApJ, 542, 224
Dopita, M. A., Sutherland, R. S., Nicholls, D. C., Kewley, L. J., & Vogt, F. P. A. 2013, ApJS, 208, 10
Erb, D. K., Pettini, M., Shapley, A. E., et al. 2010, ApJ, 719, 1168
Erb, D. K., Shapley, A. E., Pettini, M., et al. 2006, ApJ, 644, 813
Förster Schreiber, N. M., Genzel, R., Lehnert, M. D., et al. 2006, ApJ, 645, 1062
Genzel, R., Burkert, A., Bouché, N., et al. 2008, ApJ, 687, 59
Genzel, R., Newman, S., Jones, T., et al. 2011, ApJ, 733, 101
Grazian, A., Salimbeni, S., Pentericci, L., et al. 2007, A&A, 465, 393
Hainline, K. N., Shapley, A. E., Kornei, K. A., et al. 2009, ApJ, 701, 52
Hathi, N. P., Ryan, Jr., R. E., Cohen, S. H., et al. 2010, ApJ, 720, 1708
Henry, A., Scarlata, C., Domínguez, A., et al. 2013, ApJ, 776, L27
Henry, R. B. C., Edmunds, M. G., & Köppen, J. 2000, ApJ, 541, 660
Holden, B. P., Oesch, P. A., Gonzalez, V. G., et al. 2014, ArXiv e-prints
Kauffmann, G., Heckman, T. M., Tremonti, C., et al. 2003, MNRAS, 346, 1055
Kelson, D. D. 2003, PASP, 115, 688
Kennicutt, Jr., R. C. 1998, ARA&A, 36, 189
Kewley, L. J., & Dopita, M. A. 2002, ApJS, 142, 35
Kewley, L. J., Dopita, M. A., Leitherer, C., et al. 2013a, ApJ, 774, 100
Kewley, L. J., & Ellison, S. L. 2008, ApJ, 681, 1183
Kewley, L. J., Maier, C., Yabe, K., et al. 2013b, ArXiv e-prints

Kimble, R. A., MacKenty, J. W., O'Connell, R. W., & Townsend, J. A. 2008, in Society of Photo-Optical Instrumentation Engineers (SPIE) Conference Series, Vol. 7010, Society of Photo-Optical Instrumentation Engineers (SPIE) Conference Series
Kobulnicky, H. A., & Kewley, L. J. 2004, ApJ, 617, 240
Kobulnicky, H. A., Skillman, E. D., Roy, J.-R., Walsh, J. R., & Rosa, M. R. 1997, ApJ, 477, 679
Köppen, J., & Hensler, G. 2005, A&A, 434, 531
Law, D. R., Steidel, C. C., Erb, D. K., et al. 2009, ApJ, 697, 2057
Leitherer, C. 2008, in IAU Symposium, Vol. 255, IAU Symposium, ed. L. K. Hunt, S. C. Madden, & R. Schneider, 305–309
Lequeux, J., Peimbert, M., Rayo, J. F., Serrano, A., & Torres-Peimbert, S. 1979, A&A, 80, 155
Levesque, E. M., Kewley, L. J., & Larson, K. L. 2010, AJ, 139, 712
Levesque, E. M., Leitherer, C., Ekstrom, S., Meynet, G., & Schaerer, D. 2012, ApJ, 751, 67
Levesque, E. M., & Richardson, M. L. A. 2013, ArXiv e-prints
Liang, Y. C., Yin, S. Y., Hammer, F., et al. 2006, ApJ, 652, 257
Liu, X., Shapley, A. E., Coil, A. L., Brinchmann, J., & Ma, C.-P. 2008, ApJ, 678, 758
López-Sánchez, Á. R., & Esteban, C. 2010, A&A, 517, A85
Ly, C., Malkan, M. A., Hayashi, M., et al. 2011, ApJ, 735, 91
Markwardt, C. B. 2009, in Astronomical Society of the Pacific Conference Series, Vol. 411, Astronomical Data Analysis Software and Systems XVIII, ed. D. A. Bohlender, D. Durand, & P. Dowler, 251
Maseda, M. V., van der Wel, A., da Cunha, E., et al. 2013, ArXiv e-prints
McGaugh, S. S. 1991, ApJ, 380, 140
Momcheva, I. G., Lee, J. C., Ly, C., et al. 2013, AJ, 145, 47
Nakajima, K., Ouchi, M., Shimasaku, K., et al. 2013, ApJ, 769, 3
Newman, S. F., Buschkamp, P., Genzel, R., et al. 2013, ArXiv e-prints
Osterbrock, D. E., & Ferland, G. J. 2006, Astrophysics of gaseous nebulae and active galactic nuclei
Pagel, B. E. J., Edmunds, M. G., Blackwell, D. E., Chun, M. S., & Smith, G. 1979, MNRAS, 189, 95
Pagel, B. E. J., Terlevich, R. J., & Melnick, J. 1986, PASP, 98, 1005
Pérez-Montero, E., & Contini, T. 2009, MNRAS, 398, 949
Pettini, M., & Pagel, B. E. J. 2004, MNRAS, 348, L59
Pettini, M., Shapley, A. E., Steidel, C. C., et al. 2001, ApJ, 554, 981
Quadri, R., Marchesini, D., van Dokkum, P., et al. 2007, AJ, 134, 1103
Reddy, N. A., Erb, D. K., Steidel, C. C., et al. 2005, ApJ, 633, 748
Richard, J., Jones, T., Ellis, R., et al. 2011, MNRAS, 413, 643
Richardson, M. L. A., Levesque, E. M., McLinden, E. M., et al. 2013, ArXiv e-prints
Rigby, J. R., Wuyts, E., Gladders, M. D., Sharon, K., & Becker, G. D. 2011, ApJ, 732, 59
Shapley, A. E., Coil, A. L., Ma, C.-P., & Bundy, K. 2005, ApJ, 635, 1006
Shapley, A. E., Steidel, C. C., Pettini, M., & Adelberger, K. L. 2003, ApJ, 588, 65
Shim, H., Chary, R.-R., Dickinson, M., et al. 2011, ApJ, 738, 69
Shirazi, M., Brinchmann, J., & Rahmati, A. 2013, ArXiv e-prints
Simcoe, R. A., Burgasser, A. J., Bernstein, R. A., et al. 2008, in Society of Photo-Optical Instrumentation Engineers (SPIE) Conference Series, Vol. 7014, Society of Photo-Optical Instrumentation Engineers (SPIE) Conference Series
Simcoe, R. A., Burgasser, A. J., Bochanski, J. J., et al. 2010, in Society of Photo-Optical Instrumentation Engineers (SPIE) Conference Series, Vol. 7735, Society of Photo-Optical Instrumentation Engineers (SPIE) Conference Series
Skillman, E. D. 1989, ApJ, 347, 883
Steidel, C. C., Shapley, A. E., Pettini, M., et al. 2004, ApJ, 604, 534
Straughn, A. N., Kuntschner, H., Kümmel, M., et al. 2011, AJ, 141, 14
Thurston, T. R., Edmunds, M. G., & Henry, R. B. C. 1996, MNRAS, 283, 990
Tremonti, C. A., Heckman, T. M., Kauffmann, G., et al. 2004, ApJ, 613, 898
Trump, J. R., Weiner, B. J., Scarlata, C., et al. 2011, ApJ, 743, 144
Trump, J. R., Konidaris, N. P., Barro, G., et al. 2013, ApJ, 763, L6
van der Wel, A., Straughn, A. N., Rix, H.-W., et al. 2011, ApJ, 742, 111
van Zee, L., & Haynes, M. P. 2006, ApJ, 636, 214
van Zee, L., Salzer, J. J., Haynes, M. P., O'Donoghue, A. A., & Balonek, T. J. 1998, AJ, 116, 2805
Veilleux, S., & Osterbrock, D. E. 1987, ApJS, 63, 295
Villar, V., Gallego, J., Pérez-González, P. G., et al. 2008, ApJ, 677, 169
Walsh, J. R., & Roy, J.-R. 1987, ApJ, 319, L57
Welch, G. A. 1970, ApJ, 161, 821
Westmoquette, M. S., James, B., Monreal-Ibero, A., & Walsh, J. R. 2013, A&A, 550, A88
Wuyts, E., Rigby, J. R., Gladders, M. D., et al. 2012, ApJ, 745, 86
Zaritsky, D., Kennicutt, Jr., R. C., & Huchra, J. P. 1994, ApJ, 420, 87

APPENDIX

WFC3 DATA AND FIRE SPECTRA

Here we show the WFC3 grism spectra, direct H-band images, and measured lines from FIRE spectroscopy for the sample.

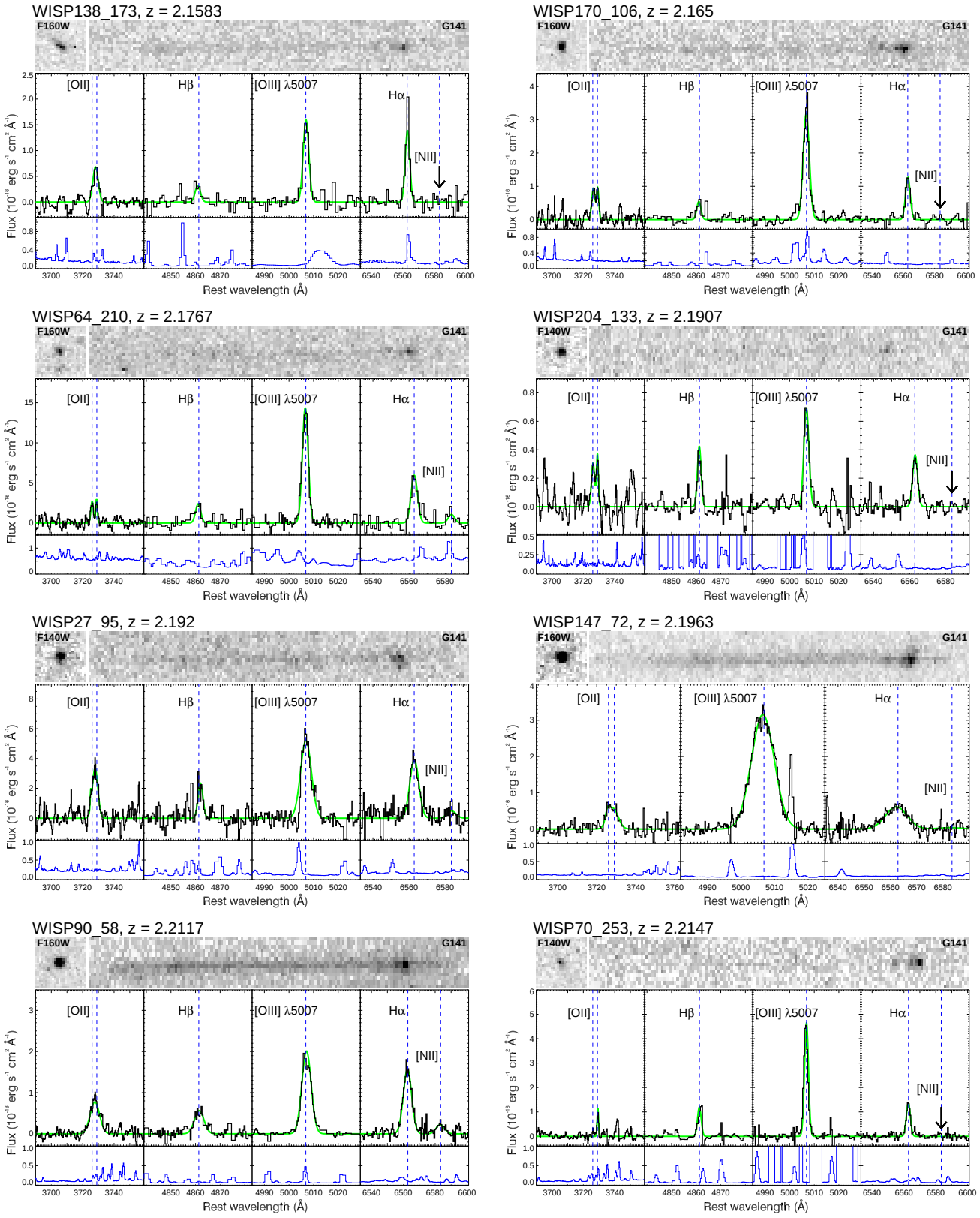

FIG. 13.— Summary of the $z \sim 2.2$ sources selected from the WISP survey for follow-up spectroscopy with FIRE. For each object we show the WFC3 direct image and grism spectrum (with clear [O III] emission, the basis of the selection) on top and the 1D emission lines measured from the FIRE spectroscopy on the bottom (the 2D grism spectrum is not on the same wavelength scale as the 1D FIRE spectrum). The error spectra are shown in the lower panels. Fits to the emission lines are shown in green. Non-detections of [N II]λ6583 are indicated with down arrows. When lines are not shown they typically were not measurable due to interference from OH sky emission lines.

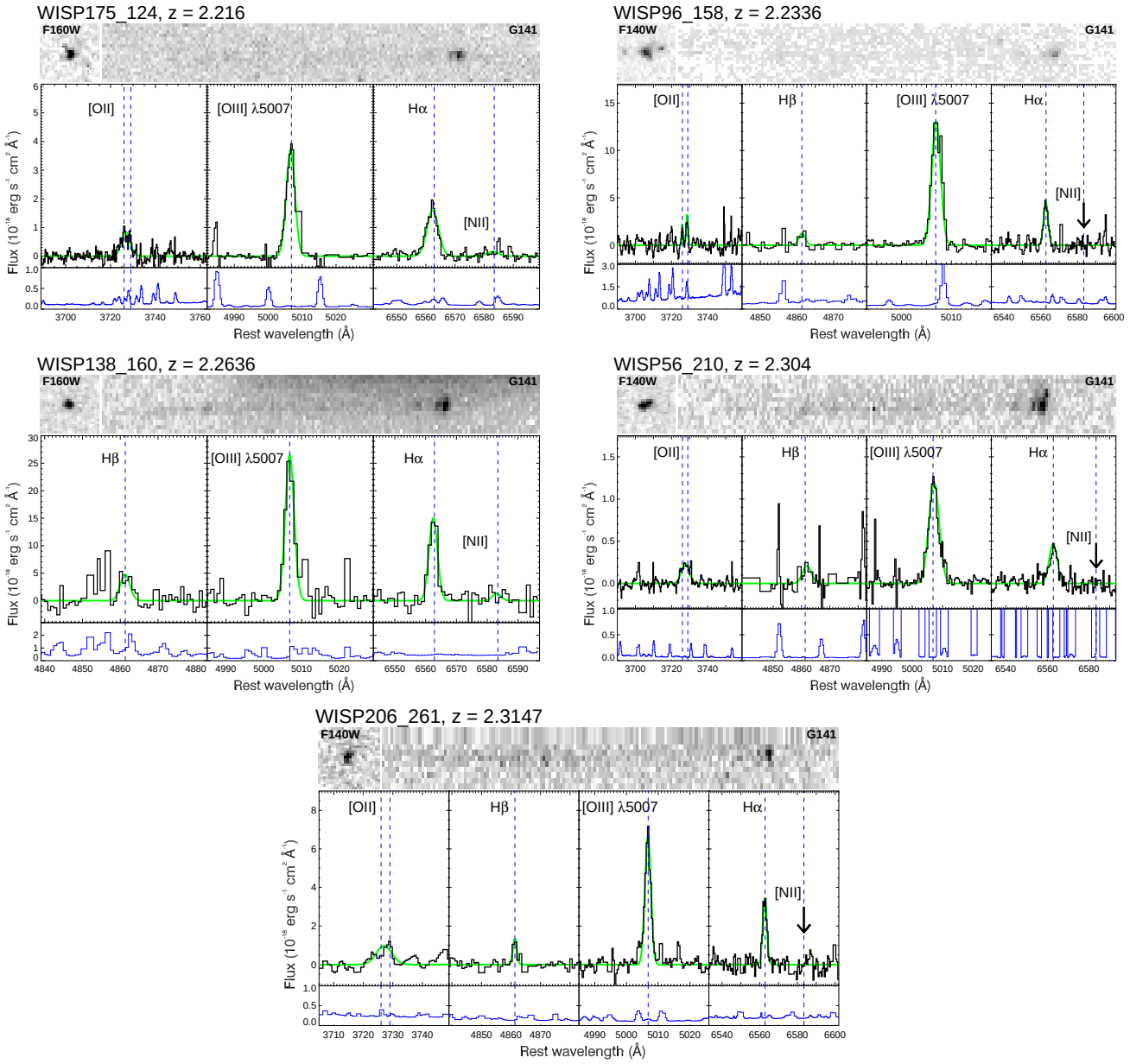

FIG. 14.— Same as for Figure 13.

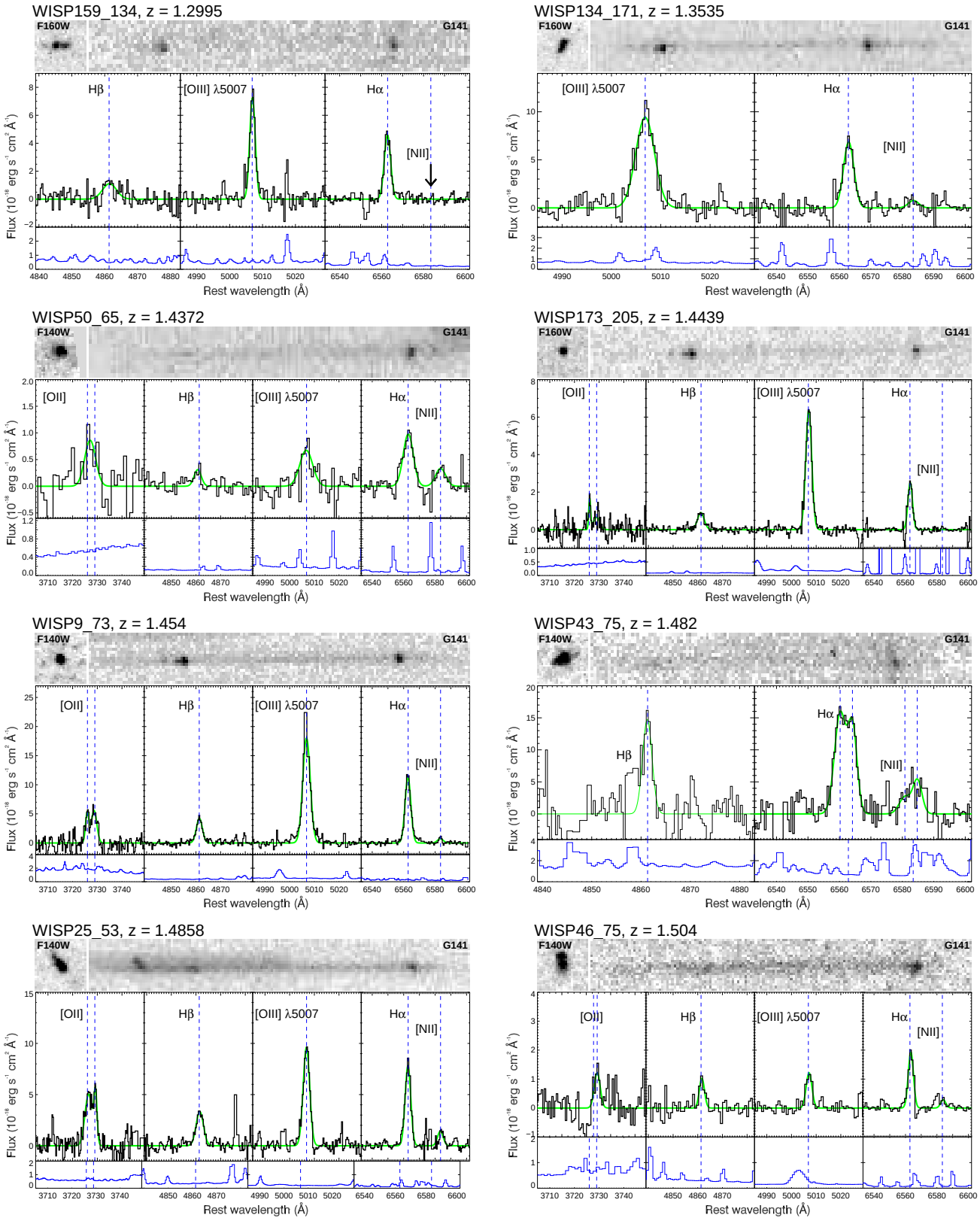

FIG. 15.— Summary of the $z \sim 1.5$ sample, as in Figures 13 and 14. In the G141 grism images both [O III] and Hα are visible for most objects.

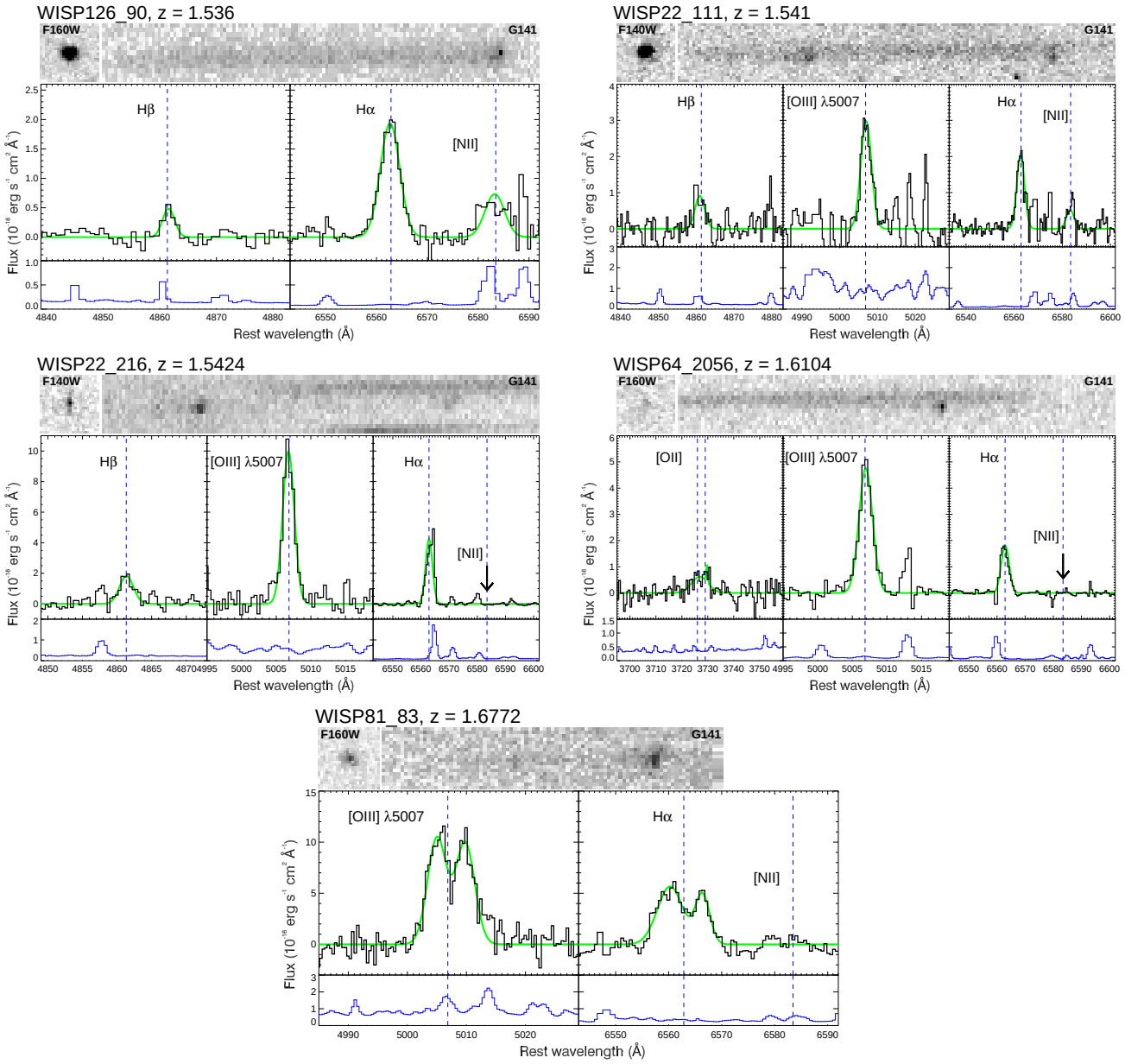

FIG. 16.— Same as for Figure 15.